International Journal of Biological Macromolecules 366 (2026) 152185

Contents lists available at ScienceDirect

International Journal of Biological Macromolecules

journal homepage: www.elsevier.com/locate/ijbiomac

Predicting the success of an antibody: Biochemical and biophysical characterization of the humanized monoclonal antibody Dia-T51

Tania Vanzolini [a,*], Valentina Fiori [b], Tomas Di Mambro [b], Mauro Magnani [a]

[a] Department of Biomolecular Sciences, University of Urbino Carlo Bo, Via Ca' Le Suore 2, 61029, Urbino, PU, Italy
[b] Diatheva s.r.l., Via Sant'Anna 131/135, 61030, Cartoceto, PU, Italy

ARTICLE INFO

Keywords:
Fungal infections
Stability
Surface plasmon resonance
UV–visible and fluorescence spectroscopy
Circular dichroism
ELISA
Dynamic light scattering

ABSTRACT

Developing effective antibody therapeutics requires not only high affinity, specificity, and potency but also optimal stability and safety. Comprehensive biophysical and biochemical profiling acts as an essential gatekeeper to predict the fate of a candidate and facilitate the transition from bench to bedside. This study evaluates the developability of Dia-T51, an anti-β-1,3-glucan monoclonal antibody humanized from the murine parental 2G8 and designed for antifungal therapy. We employed a multi-technique approach combining UV–Visible, Fluorescence, and Circular Dichroism spectroscopy with *in silico* molecular modeling to elucidate the mechanisms involved in antigen binding. Our analysis revealed a fundamental divergence between the "conformational frustration" and thermodynamic strain exhibited by 2G8 and the cooperative "induced fit" mechanism facilitated by the backbone plasticity of Dia-T51. This structural adaptability resulted in superior affinity and thermal stability for the Dia-T51-antigen complex compared to its murine counterpart. Complementary stability assessments demonstrated that Dia-T51 remains free of aggregates and undergoes a structural refinement under physiological stress. Furthermore, samples from a 3-year-old stock of Dia-T51 were subjected to accelerated stability testing to challenge *in silico* predictions of chemical liabilities within the variable regions. Despite the emergence of minor stress-related structural markers detected by Dynamic Light Scattering and SDS-PAGE, the antibody retained a predominant monomeric profile and high antigen-binding capacity, as confirmed by Surface Plasmon Resonance and ELISA. These findings demonstrate that Dia-T51 possesses the structural resilience and functional robustness required for successful clinical translation, validating its potential for downstream pharmaceutical development and the importance of integrating biophysical data into developability assessments.

1. Introduction

From the real beginning of the biotechnological era and the landmark 1986 FDA approval of muromonab (Orthoclone®), the first monoclonal antibody (mAb), the quest for the "magic bullet" significantly accelerated [1]. This surge has driven substantial efforts across the pharmaceutical industry to develop mAbs targeting unmet medical needs and bringing innovation to the therapy and diagnostics of established diseases [2,3]. However, the true 'developability' of a biologic extends far beyond mere efficacy and safety [4,5]. Thousands of promising mAbs have failed to make the transition 'from bench to bedside' due to complex intrinsic challenges. Key aspects of hit characterization, such as specificity, selectivity, potency, manufacturability, and physicochemical behavior, are critical determinants [6–8]. In this context, having deep insights into the biophysical and biochemical profile early in development is not gathering ancillary data, but rather an indispensable demonstration of approval feasibility. This information provides a fast, low-cost, and robust clue about the destiny of the antibody, thereby adhering to the principle of "fail fast and fail cheap" by reducing overall development time and costs.

A critical area of unmet medical need – where the development of such rigorously characterized novel mAbs is urgently required - is the management of infectious diseases, particularly the escalating crisis of invasive fungal infections. Recent epidemiological reassessments estimate an alarming global burden of over 6.5 million life-threatening fungal infections annually, resulting in approximately 3.8 million deaths [9]. This staggering mortality rate is primarily driven by species belonging to the *Candida*, *Aspergillus*, and *Cryptococcus* genera. The World Health Organization (WHO) recently highlighted this health threat by releasing its first Fungal Priority Pathogens List, warning

* Corresponding author at: University of Urbino Carlo Bo, Via Ca' Le Suore 2, 61029, Urbino, PU, Italy.
E-mail address: tania.vanzolini@uniurb.it (T. Vanzolini).

https://doi.org/10.1016/j.ijbiomac.2026.152185
Received 9 February 2026; Received in revised form 19 April 2026; Accepted 21 April 2026
Available online 5 May 2026

against the global spread of multidrug-resistant isolates. A paradigmatic example is the emergence is *Candidozyma auris*, a healthcare-associated pathogen that frequently exhibits multi- and pan-resistance to available drugs and causes invasive candidiasis with mortality rates often exceeding 60% [10]. Furthermore, the increasing number of immunocompromised patients - due to intensive cancer therapies, organ transplantations, and the recent surge in viral pandemic-associated co-infections - creates a continuously expanding susceptible population, transforming both novel emerging and historically re-emerging fungal species into formidable clinical challenges [10,11].

Despite the increasing incidence of fungal infections, the clinical arsenal remains severely constrained. Currently, antifungal therapy relies almost exclusively on three primary classes: polyenes, azoles, and echinocandins [12]. The clinical efficacy of these drugs is frequently compromised by severe dose-limiting toxicities, unfavorable drug-drug interactions, and narrow therapeutic windows. Most concerning is the intense selection pressure driving the rise of antifungal resistance, rendering standard treatments increasingly ineffective. This therapeutic bottleneck is drastically exacerbated by profound limitations in clinical diagnostics. Current gold-standard methods are slow, generally lack sensitivity and suffer from false positives [12]. As a result, targeted therapy is often delayed, forcing clinicians to rely on empirical treatments which significantly reduce patient survival probabilities [13].

Given the critical shortcomings of conventional antifungals, targeted passive immunotherapy *via* monoclonal antibodies (mAbs) represents a highly promising alternative. Among fungal structural components, β-1,3-glucan is an ideal target: it is an essential architectural polysaccharide highly conserved across a vast array of fungal cell walls, yet entirely absent in mammalian tissues, guaranteeing excellent pharmacological selectivity [14]. Over the years, a few murine mAbs directed against β-glucans have been described, validating the druggability of this antigen. For instance, the murine mAbs AG and BG were developed to specifically recognize β-1,3-1,6-glucan linkages on intact *Candida* and *Cryptococcus* cells, proving highly valuable primarily for diagnostic recognition assays [15]. Similarly, the mouse mAbs 3G11 and 5H5 have shown high specific affinity for β-1,3-glucan, successfully demonstrating targeted *in vitro* neutralizing activity by inhibiting *C. albicans* cellular growth and *A. fumigatus* spore germination [16]. Another example is the 1E12 clone, which exhibited both *in vitro* and *in vivo* antifungal activity; however, its clinical development is intrinsically hindered by its IgM isotype, a large pentameric structure that severely limits deep tissue penetration and poses major manufacturability challenges [17,18].

While these clones highlight the therapeutic potential of targeting β-glucans, the most extensively characterized and promising antibody remains the murine 2G8 (IgG2b). 2G8 has demonstrated remarkable broad-spectrum antifungal capabilities. *In vitro* and *in vivo* studies have proven that 2G8 specifically binds to the cell walls of major human pathogens, including *C. albicans*, *A. fumigatus*, and *C. neoformans*, directly inhibiting fungal growth and conferring significant passive protection in experimental models of systemic infection [17,19,20]. Nevertheless, despite these successes, the clinical translation of 2G8 - and its aforementioned mAbs - is fundamentally precluded by their non-human origin. Systemic administration of mouse-derived immunoglobulins inevitably elicits human anti-mouse antibody (HAMA) responses, leading to rapid drug clearance, neutralization, and unacceptable hypersensitivity risks [21]. This strict biological limitation dictates the indispensable need for humanized counterparts, such as Dia-T51.

Dia-T51 (IgG1) was strategically humanized from the 2G8 progenitor [22,23]. Preclinical evaluations have demonstrated that this process not only preserved but significantly improved target recognition. Biologically, Dia-T51 has demonstrated potent, dose-dependent antifungal efficacy *in vitro* against the critical-threat pathogen *C. auris*. It significantly inhibits fungal growth and adhesion and strengthens phagocytosis. Furthermore, beyond its direct neutralizing capabilities as a standalone agent, Dia-T51 exhibits remarkable synergistic potential when co-administered with current standard-of-care antifungals, such as amphotericin B and caspofungin, effectively enhancing their fungal clearance and offering a strategy to lower their clinical dosages to mitigate toxicities [22,24]. These findings were successfully translated *in vivo*, where Dia-T51 treatment markedly improved survival rates in *Galleria mellonella* infection models when administered both as a prophylactic and therapeutic agent, and both alone and in combination with amphotericin B [25].

However, in the highly demanding landscape of modern biotherapeutics, superior target binding and *in vitro/in vivo* efficacy are necessary but entirely insufficient for clinical approval. The transition from a highly potent lead molecule to an approved biologic is increasingly ruled by its "developability", a rigorous multi-parametric screening profile designed to ensure that a candidate can pass through Chemistry, Manufacturing, and Control (CMC) stages without late-stage attrition [26–28]. A comprehensive developability assessment requires the evaluation of several interconnected biophysical and biochemical liabilities [4]. The foremost parameters are conformational and thermodynamic stability which act as predictors of an antibody's shelf-life and structural resilience. Candidates prone to premature unfolding under physiological, thermal, or mechanical stress, risk aggregation and loss of colloidal stability [4]. This not only compromises drug solubility but can trigger severe immunogenic responses, a primary cause of immediate clinical failure [4,29,30]. Additionally, antibodies face spontaneous chemical liabilities during long-term storage, including oxidation, deamidation, and fragmentation, which can severely alter the paratope integrity and negatively impact batch-to-batch consistency [26]. Finally, these biophysical constraints dictate manufacturability, as therapeutic mAbs must often endure high formulation concentrations without precipitating or becoming excessively viscous [31]. Recent large-scale evaluations of the clinical-stage landscape explicitly highlight that anomalies in these intrinsic physical properties, rather than poor target affinity, are the primary drivers of late-stage clinical attrition [4]. Within this strict conceptual framework, understanding the structural resilience of Dia-T51 is not merely descriptive, but fundamentally predictive of its clinical fate. A comprehensive biophysical and biochemical profiling is strictly required to ensure that it aligns with the stringent safety and manufacturability guidelines of regulatory agencies. Moreover, neither Dia-T51 nor its murine parent has been thoroughly explored in these fundamental areas. Hence, the primary objective of this manuscript is to supply this missing knowledge. To achieve this, Dia-T51 was extensively characterized, with comparative analysis against the parental murine mAb 2G8 in selected cases. The multidimensional analytical approach employed in our study encompassed various spectroscopic, biophysical and biochemical techniques [32]: UV–visible and fluorescence spectroscopy were used to investigate the secondary and tertiary structure and monitor the conformational changes upon antigen binding. With circular dichroism (CD) we further assessed secondary/tertiary structure and determined the melting temperature with and without the antibody-antigen complex. SDS-PAGE and dynamic light scattering (DLS) were useful to observe the mAb stability when subjected to prolonged incubation at 37 °C [32]. Enzyme-Linked ImmunoSorbent Assay (ELISA) and Surface Plasmon Resonance (SPR) were employed to study the binding affinity and kinetics after 3-years storage period, providing a measure of functional stability. In parallel, Congo Red and proteolytic assays on newly produced batches of Dia-T51 confirmed the absence of aggregates even after several days of incubation at 37 °C.

These specific experimental evaluations provide the indispensable, predictive evidence required to validate Dia-T51 not just as a potent target binder, but as a robust, clinical-grade therapeutic candidate fully equipped to withstand the rigorous demands of pharmaceutical manufacturing and patient administration.

2. Material and methods

2.1. Materials

Dia-T51 and 2G8 antibodies were kindly provided by Diatheva s.r.l. as research grade products. Laminarin (from *Laminaria digitata*) was purchased from Sigma-Aldrich (Cat. No. L9634). The buffers used in this study were: 20 mM Tris-HCl, 0.15 M NaF, pH 7.4 for spectroscopic analyses (UV–Vis, fluorescence and CD), 1× HBS-EP+ buffer, pH 7.4 (Cytiva) for SPR analyses and Phosphate Buffered Saline (PBS - 8 g/l NaCl, 0.2 g/l KH_2PO_4, 2.9 g/l $Na_2HPO_4{\cdot}12H_2O$, 0.2 g/l KCl, pH 7.4) for storage and stability studies.

2.2. UV–vis spectroscopy

UV–Visible absorbance spectra were acquired in the 600–200 nm range using a double-beam Varian Cary-100 spectrophotometer equipped with a temperature control unit. Measurements were performed at 25 °C. Antibodies were analyzed at a concentration of 0.05 mg/ml, using the corresponding buffer as a reference in the second cell path. For saturation assays with the laminarin antigen, molar ratios were used. Since laminarin exhibits intrinsic absorbance, spectra were corrected by subtracting the laminarin baseline signal to distinguish antibody contributions from non-specific optical effects. Data analysis, including the calculation of second derivative spectra, was performed using OriginPro software.

2.3. Fluorescence spectroscopy

Intrinsic fluorescence emission spectra were recorded at 25 °C using a Varian Cary Eclipse spectrofluorimeter. Antibodies were analyzed at a concentration of 0.05 mg/ml. Tryptophan emission spectra were collected from 600 to 285 nm following excitation at 280 nm and using an emission filter (1100–295 nm range) to reduce scattering. For saturation assay, small aliquots of a concentrated laminarin stock solution were added to the antibody sample; the total added volume was kept below 5% to minimize dilution effects. Data analysis was performed using OriginPro software.

2.4. Circular dichroism (CD)

Far-UV CD spectra were recorded using a Jasco J1000 spectropolarimeter. Analyses were performed at 25 °C in a 0.3 mm pathlength quartz cell using an antibody concentration of 0.1 mg/ml in the 260–190 nm wavelength range. Secondary structure content was estimated using the BeStSel web server (https://bestsel.elte.hu/) [33–35]. For titration experiments, the signal of laminarin was subtracted prior to data analysis. Thermal denaturation studies were performed by applying a temperature gradient from 20 °C to 100 °C, with a heating rate of 10 °C/min and data acquisition every 5 °C. Thermal stability data were analyzed using the Jasco evaluation software. To specifically determine the melting temperature (Tm), the loss of β-sheet secondary structure was monitored at the characteristic 215–216.5 nm negative peak. Because the Dia-T51 complex with laminarin exhibited exceptional stability and did not reach full denaturation at 100 °C, an extended thermal scan up to 130 °C was performed to completely resolve its unfolding transition.

The resulting thermal unfolding curves were analyzed using GraphPad Prism software by fitting the data to a Boltzmann sigmoidal equation. The apparent melting temperature was mathematically extracted as the inflection point of the fitted sigmoid. Finally, the thermal shift (ΔTm) was calculated as the difference between the Tm of the antigen-complexed and the free antibody states.

2.5. Surface Plasmon Resonance (SPR)

Binding kinetics and affinity were assessed using a Biacore 1 K instrument (Cytiva). Antibodies were immobilized on a Protein A Sensor Chip Series S (Cytiva). For Dia-T51 HBS-EP+ buffer (150 mM NaCl, 10 mM HEPES pH 7.4, 3 mM EDTA, 0.05% Surfactant P20) was used for both the dilution and running conditions. For the murine 2G8 antibody, initial capture at physiological pH was unstable, coherent with the known weak affinity of murine IgG Fc regions for Staphylococcal Protein A at neutral pH [36,37]. To establish a stable baseline, a systematic buffer scouting was performed testing PBS at different ionic strengths (0.15 M and 0.3 M NaCl) and pH values (6.5, 7.5, 8.5). The most stable capture was achieved using high-salt (0.3 M NaCl) PBS at pH 8.5. Furthermore, to validate the assay and rule out mass transport limitations or avidity artifacts, antigen binding was evaluated at multiple antibody capture levels. The resulting kinetic parameters were largely overlapping and consistent regardless of the surface density, demonstrating density-independence and confirming the optimality of the chosen conditions. During the kinetic assays, laminarin was injected into flow cell 2, while flow cell 1 served as the reference surface. Antibody concentration was finally fixed at 1 μg/ml (assuming an MW of 150 kDa). For laminarin, an approximate molecular weight of 6 kDa (based on literature [38] and the reported 5–8.6 kDa range for *L. digitata* in Sigma-Aldrich product information) was used for calculations. Laminarin was injected at concentrations of 0.68, 2.04, 6.15, 18.44, 55.33, and 166 nM at 25 °C. Data were analyzed using the Biacore 1 K Evaluation Software, fitting the curves to a 1:1 binding model after reference subtraction.

2.6. In silico structural modeling and liability analysis

The three-dimensional structures of the antibody variable regions were predicted using ABodyBuilder2 (Oxford Protein Informatics Group; https://opig.stats.ox.ac.uk/webapps/sabdab-sabpred/sabpred/abodybuilder2/) [39]. The amino acid sequences of the Variable Heavy (VH) and Variable Light (VL) domains were used as input for the deep-learning pipeline, which utilizes equivariant graph neural networks for accurate backbone and side-chain prediction [40]. The resulting models were analyzed to assess developability. Structural liabilities - specifically residues prone to chemical modifications such as oxidation, deamination, and isomerization - were mapped onto the 3D models to evaluate solvent accessibility and potential stability risks.

2.7. In silico structural analysis

Protein structures (pdb files) were retrieved from the Structural Antibody Database (SabDab) and analyzed using UCSF ChimeraX (version 1.8). The Solvent Accessible Surface Area (SASA) was calculated using the standard "rolling probe" algorithm [41] with a probe radius of 1.4 Å to simulate the hydration shell of a water molecule. To visually discriminate between the hydrophobic core and the hydrophilic exterior, a discrete color gradient was established based on absolute area values ($Å^2$): buried threshold (0–25 $Å^{2)}$: residues with a SASA $\leq$25 $Å^2$ were classified as buried and colored orange. This cutoff aligns with the structural definition of the hydrophobic core, where residues exhibit minimal contact with the solvent [42]. Exposed threshold (>25 $Å^2$): residues exceeding this threshold were classified as solvent-accessible and colored blue. The upper limit for gradient saturation was set to 50 $Å^2$ to maximize visual contrast at the buried/exposed boundary, ensuring that residues with intermediate exposure are clearly distinguishable from the fully solvated surface. For the structural comparison the variable domains of Dia-T51 and 2G8 were superimposed. Surface transparency was rendered to reveal the internal packing of the VL/VH interface. Electrostatic surface potentials were computed using the Coulombic surface coloring module in ChimeraX. The potential (φ) was calculated following Coulomb's law. The color scale was normalized to a

range of −10 kcal/(mol·e) (red, electronegative) to +10 kcal/(mol·e) (blue, electropositive).

2.8. ELISA assay

A 96-well-plate was coated overnight at 4 °C with 50 μg/ml laminarin in 0.05 M carbonate buffer (pH 9.6). Nonspecific interactions were avoided with blocking solution, 3% (*w*/*v*) Bovine Serum Albumin (BSA) in PBS containing 0.05% (*v*/v) Tween 20 (pH 7.4) for 1 h at 37 °C. Dia-T51 samples from the stability test (3-years old and stored at 37 °C for varying durations) were diluted in blocking solution (from 3.125 to 0.006 μg/ml), added to the wells, and incubated for 2 h at 37 °C. After washing, wells were incubated for 1 h at 37 °C with Goat anti-human-HRP (Meridian Life Science, Inc., G5G16–0482) diluted 1:500 in blocking solution. Signal detection was performed using a 5 mg-ABTS tablet (Roche Diagnostics) dissolved in 12 ml of 0.05 M sodium citrate (pH 3) supplemented with hydrogen peroxide (Carlo Erba - 1:1000 dilution). Absorbance at 405 nm was measured with a Microplate Reader (Bio-Rad) after 15, 30, 45 and 60 min. Washing steps were performed between each stage. Data was analyzed using GraphPad Prism.

2.9. SDS-PAGE

Dia-T51 aliquots from the stability test were diluted in SDS sample buffer either with or without 4% (*v*/v) β-mercaptoethanol, vortexed and heated at 100 °C for 3 min. Proteins were resolved onto SDS-PAGE polyacrylamide gels and stained with Brilliant Blue Coomassie R-250.

2.10. Dynamic Light Scattering (DLS)

Aggregation state and colloidal stability of Dia-T51 samples from the stability test were evaluated using a Malvern Zetasizer Nano S (Malvern Instruments Ltd., UK). Samples were measured at a concentration of 0.1 mg/ml. The hydrodynamic diameter, area of the peaks and Polydispersity Index (PdI) were recorded to monitor particle size distribution and potential degradation.

2.11. Congo Red binding assay

To assess the potential formation of amyloid-like aggregates, a Congo Red spectroscopic assay was performed on a freshly produced batch of Dia-T51. Samples were evaluated over a 14-day incubation period at 37 °C (Day 0, Day 7, and Day 14). Heat-aggregated (80 °C for 30 min.) bovine serum albumin (BSA) (Sigma-Aldrich) was used as a positive control for amyloid-like fibril formation. Congo Red powder was solubilized in PBS, filtered through a 0.22 μm membrane, and its concentration was determined by measuring absorbance at 498 nm. Dia-T51 and BSA were diluted in PBS to a final concentration of 1 mg/ml in a 96-well plate (200 μl total volume per well). Congo Red solution was added to yield a final concentration of 20 μM. PBS alone and corresponding protein samples without Congo Red were included as parallel blank controls. The plate was incubated RT in the dark for 30 min. UV–Vis absorbance spectra were recorded from 700 to 300 nm using a FluostarOMEGA microplate reader (BMG LABTECH). Prior to data analysis, the intrinsic background absorbance of the protein samples without the dye was subtracted from the spectra of their respective Congo Red-treated samples. The presence of amyloid structures was evaluated by monitoring the characteristic red shift of the absorbance peak (from 490 nm to 540 nm) and by calculating the absorbance ratio at 540 nm and 480 nm (Abs540/Abs480).

2.12. Proteolysis assay

The structural integrity and backbone accessibility of fresh Dia-T51 were probed *via* proteolysis using pepsin (Sigma-Aldrich). Dia-T51 samples at day 0 and after 10 days of incubation at 37 °C were digested at an enzyme-to-substrate ratio of 1:50 (*w*/w) in 50 mM sodium citrate buffer (pH 3.0) at 37 °C. Aliquots were withdrawn at 5, 15, 45, and 150 min, and the reaction was immediately stopped by adding sample buffer with or without 4% (*v*/v) β-mercaptoethanol. Samples were then vortexed and heated at 100 °C for 3 min. Undigested Dia-T51 samples from both day 0 and day 10 were included as baseline controls to confirm the absence of any spontaneous thermal degradation prior to the assay. Additionally, pepsin alone at the working concentration was loaded onto the gel to ensure that all visible fragmentation bands derive exclusively from enzymatic cleavage of the antibody. Proteolytic fragments were resolved on 12% SDS-PAGE polyacrylamide gels which were stained with Coomassie Brilliant Blue R-250 and imaged using a ChemiDoc Imaging System (Bio-Rad).

3. Results and discussion

3.1. UV–visible spectroscopic analysis of antibody-antigen interaction

The UV–Visible absorbance spectra of Dia-T51 and 2G8 were acquired in the 600–200 nm range. Both antibodies exhibited a dual-peak profile: a high-intensity peak below 250 nm, primarily attributable to the $n \rightarrow \pi^*$ and $\pi \rightarrow \pi^*$ transitions of the amides in peptide bonds (respectively ~220 nm and ~ 190 nm), alongside contributions from specific amino acid side chains (Histidine, Cysteine and Methionine) and buffer components; and a second, less intense but specific peak at 279 nm, resulting from the absorption of aromatic amino acids, notably Tryptophan (Trp, ~280 nm), Tyrosine (Tyr, ~275 nm), and Phenylalanine (Phe, ~258 nm) (Fig. 1 A and B). Initial raw data indicated an apparent increase in intensity and spectral shifts proportional to laminarin concentration (data not shown). However, upon rigorous subtraction of the laminarin baseline, the zero-order spectra revealed that the global peak position (λ_{max}) and absolute intensity at 279 nm remained largely invariant. This indicates that there is no massive solvent exposure of the aromatic core. Nevertheless, the spectroscopic data provided a detailed molecular view of the binding mechanics distinguishing Dia-T51 from 2G8, revealing a complex interplay between structural organization and local adaptability. The preservation of the global spectral profile upon binding confirms that the antibody-antigen interaction does not disrupt the overall tertiary fold. Unlike denaturing events that expose the hydrophobic core, the interaction is confined to surface rearrangements, maintaining the structural integrity of the antibody scaffold.

The static nature of the zero-order profile masks fine-tuned local variations during antigen binding, which were successfully unveiled by the Foldedness Ratio and the second-derivative spectroscopy.

The Foldedness Ratio is as a sensitive probe for conformational dynamics, integrating the spectral contributions of Tyrosine and Phenylalanine alongside Tryptophan [43,44].

Typically, a reduction in the Foldedness Ratio serves as a decrease in Trp absorbance or a concomitant increase in Tyr and/or Phe signals; consequently, native conformations generally exhibit higher ratio values compared to the antigen-complexed forms.

In our study, comparisons revealed that the complexed state exhibits lower ratio values relative to the native conformation. Despite the lack of macroscopic spectral shifts, the raw absorbance data displayed a concentration-dependent hypochromic effect across all monitored wavelengths, becoming particularly prominent from the 1:400 M ratio onwards (Fig. 1C). This spectral signature suggests that while the overall globular architecture is preserved, the local microenvironment of the aromatic residues is significantly perturbed by the binding event [45]. Furthermore, the persistence of these alterations (decrease in absorbance across all three aromatic residues) at high laminarin concentrations points to the onset of non-specific interactions capable of broadly affecting the solvent accessibility of the aromatic core.

Notably, the most significant calculated differences involve

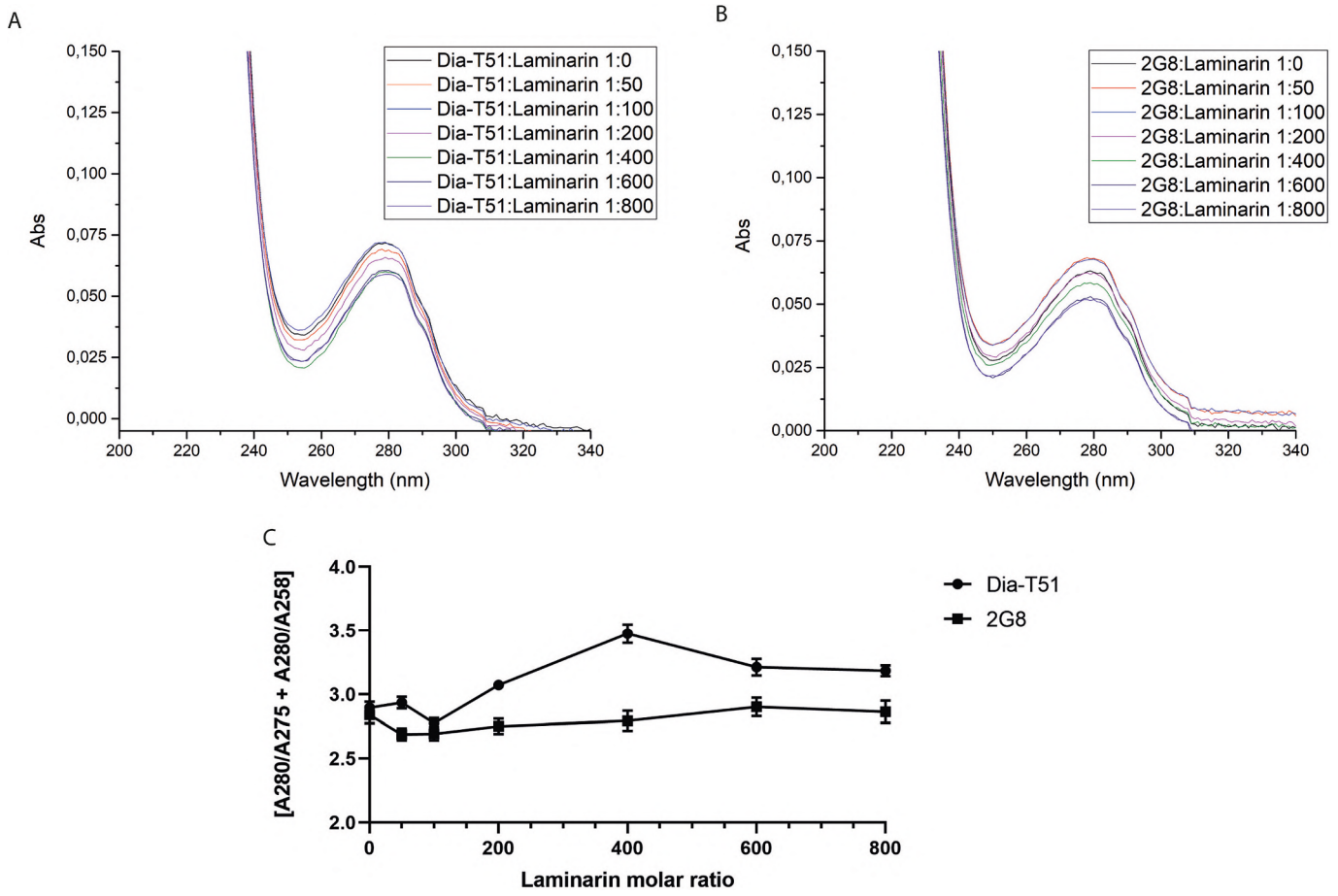

Fig. 1. UV absorbance spectra with antigen titration and analysis of conformational changes *via* Foldedness Ratio. Spectral changes of Dia-T51 (A) and 2G8 (B) were monitored during titration with increasing concentrations of laminarin. mAbs were diluted in PBS (pH 7.4) to the final concentration of 0.33 μM. Measurements were performed at the controlled temperature of 25 °C. The Foldedness Ratio (C), calculated from the zero-order UV spectra according to the following relationship: λT280/(λ275 + λ258), was used to monitor the aromatic core stability during antigen binding. The plot illustrates the variations in the Trp, Tyr, and Phe residue microenvironment for Dia-T51 and 2G8 upon titration with increasing molar ratios of laminarin. The shown spectra are representative of four (for Dia-T51) and six (for 2G8) independent replicates. Foldedness Ratio data were extracted from each individual replicate prior to averaging. Values represent the mean ± SD of $n = 4$ and $n = 6$ independent experiments for Dia-T51 and 2G8 mAbs respectively.

wavelengths of 280 nm and 275 nm—corresponding to Trp and Tyr, respectively—although spectral overlap between these residues must be considered. Interestingly, the analysis of the Foldedness Ratio revealed a striking divergence in the spectral contribution of Phenylalanine between the two antibodies. While the Phe signal variation in Dia-T51 paralleled that of Tryptophan and Tyrosine (data not shown), the halved spectroscopic response of Phenylalanine in 2G8 can be rationalized by its distinct topological distribution [46].

Although the positioning of Trp and Tyr remains largely conserved within the variable domains (with the exception of a single additional Tyr in the VH-Framework 4 of 2G8), the localization of Phe differs. Specifically, 2G8 possesses a unique Phe residue in VL-Framework 3 (Phe 101, Fig. 2), proximal to CDR3 which appears structurally decoupled from the primary binding event, hence resulting in the observed dampening of the signal. In contrast, Dia-T51 lacks this residue, featuring instead a Phe in VL-Framework 2 (Phe 42, Fig. 2), adjacent to CDR1 and likely integral to the dynamic interface. This divergence is further highlighted at lower molar ratios (1:50 and 1:100), where 2G8 exhibited a unique, Phe-driven hyperchromicity [47]. In contrast, Dia-T51 showed a slight absorbance decrease at 1:50 followed by an increase at 1:100. This implies different conformational behaviors: 2G8 undergoes rearrangements or compensatory spatial shifts that mask the Phe signal, whereas Dia-T51 exhibits a more direct structural response (likely involving the engagement of Phe residues), translating into the observed differences in stability and affinity.

To overcome the limited resolution of zero-order spectroscopy and further investigate these fine structural dynamics, second-derivative analysis was applied.

Spectral shifts were monitored *via* the intersections with the abscissa of the derivative signal (approximating 286, 289, and 293 nm) (Figs. 3C-E and 4C-E). Unlike the raw spectra, the second-derivative spectra allow for the resolution of overlapping bands of Tryptophan, Tyrosine, and Phenylalanine into specific wavelength displacements and intensity fluctuations [43].

At 286 nm both antibodies initially exhibit a blue shift in the complexed form. For 2G8, this occurs at a laminarin molar ratio of 1:100, whereas for Dia-T51, it appears earlier at 1:50. This trend is transient, interrupted by a red shift peaking at 1:200, followed by a reversion to a blue shift. A similar oscillatory pattern is observed at 289 nm: a blue shift peak at 1:50 (marked by a higher magnitude in Dia-T51) transitions to a red shift up to 1:200, before returning to a blue shift.

While the global aromatic environment remains protected from bulk solvent (explaining the invariant zero-order spectra), the oscillatory shifts observed at the zero-crossing points 286 and 289 nm indicate that antigen binding triggers specific micro-environmental reorganization of Tyrosine and Tryptophan residues. This suggests that the paratope is largely pre-formed but possesses the necessary local plasticity to undergo fine-tuning upon ligand docking. Conversely, the spectral

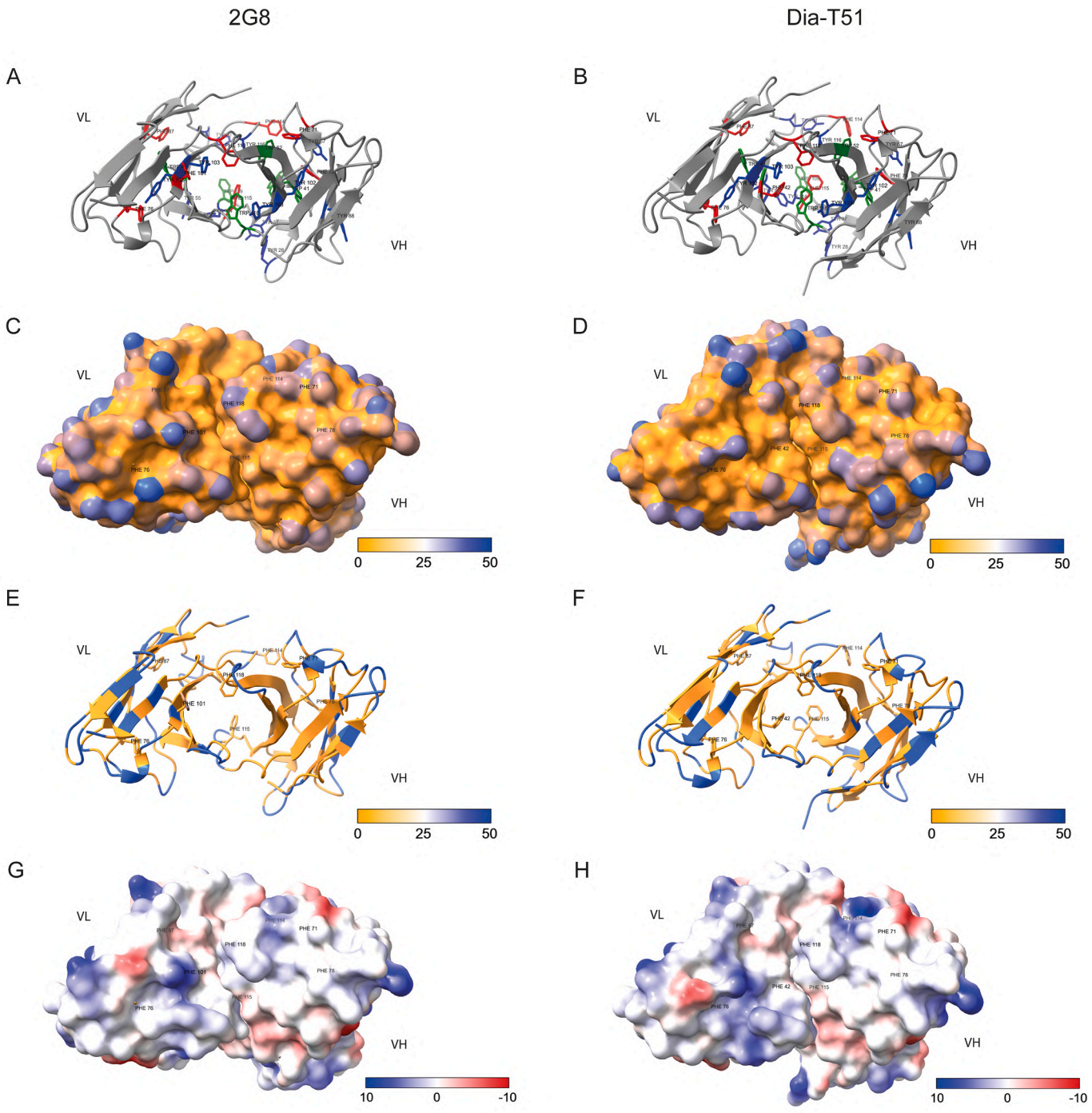

Light chain variable regions

	10	20	30	40	50	60	70	80	90	100	110	120
IMGT												
2G8	DIVMTQSPLT	LSVTIGQPAS	ISCKSSQSLL	YS-NGNTHLN	WLLQRPGQSP	KRLIYLV---	----SKLDSG	VP-DRFTGSG	--SGTDFTLK	ISRVEAEDLG	FYYCVQGTH-	---FPYTFGG GTKLEIK
Dia-T51	DVVMTQSPLS	LPVTLGQPAS	ISCRSSQSLL	YS-NGNTHLN	WFQQRPGQSP	RRLIYLV---	----SNRDSG	VP-DRFSGSG	--SGTDFTLK	ISRVEAEDVG	VYYCVQGTH-	---FPYTFGG GTKLEIK

Heavy chain variable regions

	10	20	30	40	50	60	70	80	90	100	110	120
IMGT												
2G8	---LQQSGA-	ELMKPGASVK	ISCKATGYTL	----SSYWLE	WVKQRPGHGL	EWIGEILPG-	-SGSTNYNEK	FK-GKATFTA	DTSSNTAYMQ	LSSLTSEDSA	VYYCAREGW-	---YFDVWGA GTTVTVSS
Dia-T51	QVQLQQSGA-	ELKKPGASVK	ISCKASGYTL	----SSYWLE	WVRQRPGQGL	EWIGEILPG-	-SGSTNYNEK	FK-GRATFTA	DTSTNTAYME	LSSLTSEDSA	VYYCAREGW-	---YFDVWGQ GTTVTVSS

(caption on next page)

Fig. 2. Structural characterization, solvent accessibility, and surface property analysis of variable regions of Dia-T51 *versus* 2 g8. The sequences were launched in the structural antibody database SAbDab. 3D structures were predicted by ABodyBuilder2 and analyzed in ChimeraX. (A, B) Secondary structure representation (cartoon) highlighting the distribution of aromatic residues. Side chains of Phenylalanine (Phe) in red, Tyrosine (Tyr) in blue, and Tryptophan (Trp) in green are shown as sticks to visualize packing interactions and aromatic clustering. (C, D) Solvent Accessible Surface Area (SASA) mapping. The molecular surface is colored according to absolute solvent accessibility calculated in ChimeraX. A custom gradient was applied: orange indicates buried residues ($0 \leq$ SASA ≤ 25 Å^2), while blue indicates solvent-exposed residues (SASA ≥ 25 Å^2), with color saturation set at 50 Å^2. (E, F) Detailed visualization of the secondary structure of VL/VH interface of the antibodies and core packing with transparent surface rendering but solvent accessibility gradient. The focus is on the structural discrepancy between Phenylalanine residues in Dia-T51 and 2G8. In particular, Phe 42 in Dia-T51 is deeply buried within the hydrophobic VL-VH interface, contributing to domain stability, whereas the corresponding region in 2 g8 lacks this residue, featuring instead a solvent-exposed Phe101 in a distal position. (G, H) Coulombic Electrostatic Potential (ESP) surfaces. The surface is colored by electrostatic potential calculated according to Coulomb's law: red indicates negative potential, white indicates neutral, and blue indicates positive potential. The scale bar represents potential ranging from −10 to +10 kcal/(mol·e). The sequences of VH and VL domains of the antibodies were reported and aligned according to the IMGT numbering scheme using SAbDab.

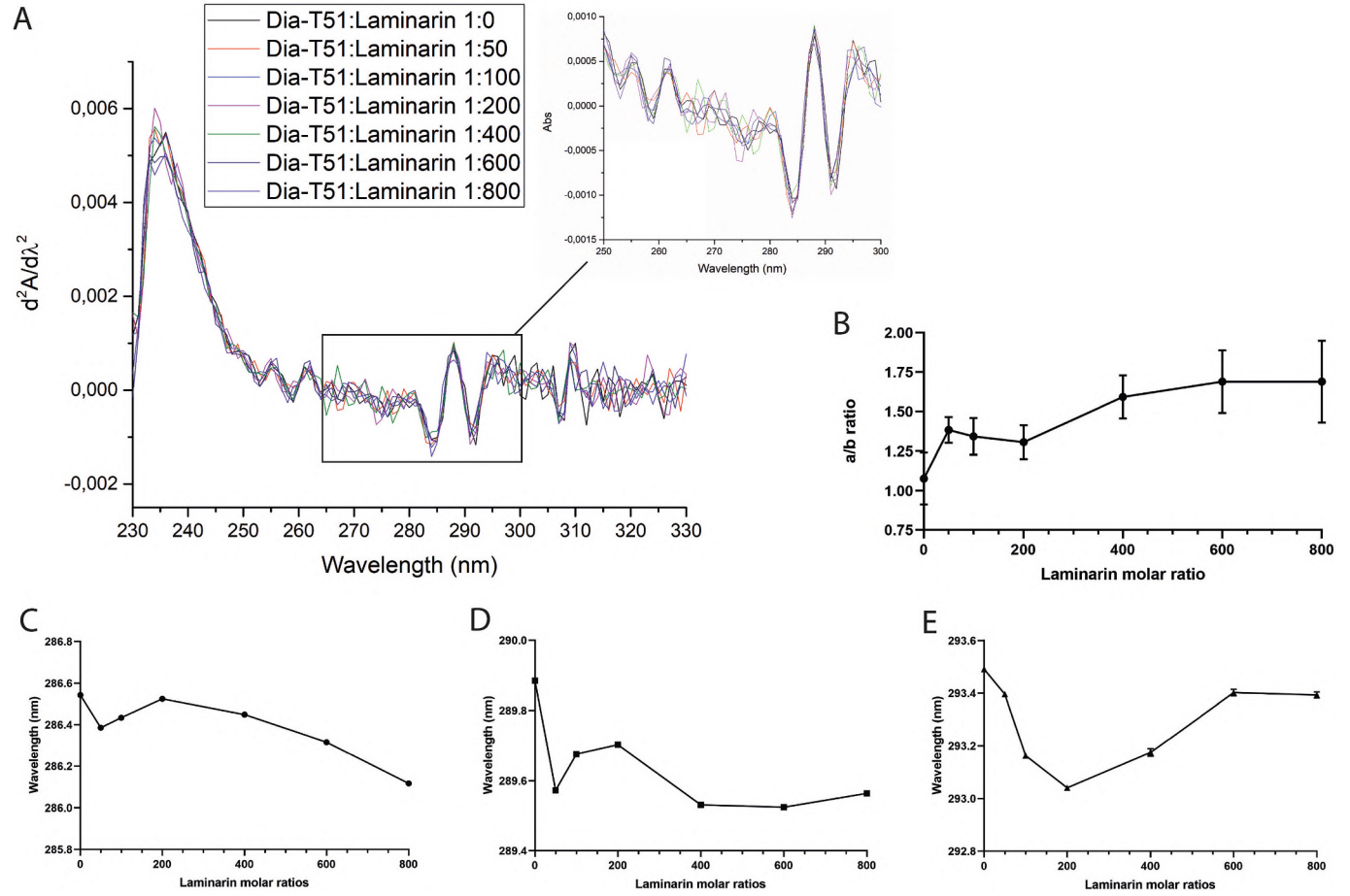

Fig. 3. Spectroscopic characterization of Dia-T51 *via* second-derivative analysis. (A) Second-order derivative spectra obtained through mathematical differentiation of zero-order signals to enhance spectral resolution. (B) a/b ratio calculated from the peak-to-trough distances of the second-derivative spectra of laminarin titration. Value a (288–283 nm) quantifies Tyrosine contribution, while value b (295–291 nm) quantifies Tryptophan contribution, used here to monitor solvent accessibility during antigen engagement. (C, D and E) Monitoring of wavelength shifts at the intersections with the abscissa axis (approximately 286, 289, and 293 nm). The displayed spectra are representative of three independent experiments. The a/b ratio and the wavelengths intersecting the abscissa axis were determined for each independent run ($n = 3$) before calculating the average. The reported values represent the mean ± SD.

evolution at 293 nm, predominantly driven by Tryptophan transitions, reveals a critical divergence in how these rearrangements occur. In both antibodies, Trp residues are largely conserved within the variable regions (within VH-CDR1 and CDR3, and proximal to VL-CRD1 and VH-CDRs). However, despite this shared topological distribution, the resulting conformational dynamics differ significantly. Dia-T51 displays a simpler biphasic response (blue shift at 1:200 followed by a red shift up to 1:600), consistent with a cooperative and orderly adjustment of the binding pocket. In sharp contrast, 2G8 exhibits complex, multiphasic shifts (red shift up to 1:100, blue at 1:200, red at 1:600, and blue at 1:800). This behavior is suggestive of "conformational frustration" [48], indicating a search for the optimal binding conformation - corresponding to an energetic minimum - through multiple intermediate states within a rugged energy landscape.

Regarding signal amplitude, 2G8 shows higher magnitude variations upon laminarin addition; specifically, from a 1:400 M ratio onwards, troughs become more negative and peaks less positive. Dia-T51 exhibits a similar but attenuated trend, characterized by a deepening of the trough at 284 nm, an intensity increase at the 288 nm peak, and a reduction in the trough at 292 nm (Figs. 3A and 4A).

To deconvolute the residues contributions, the empirical r = a/b ratio derived from derivative spectra was evaluated, where a represents the peak-to-trough distance between 288 and 283 nm (Tyr contribution) and b between 295 and 291 nm (Trp contribution) (Figs. 3B and 4B)

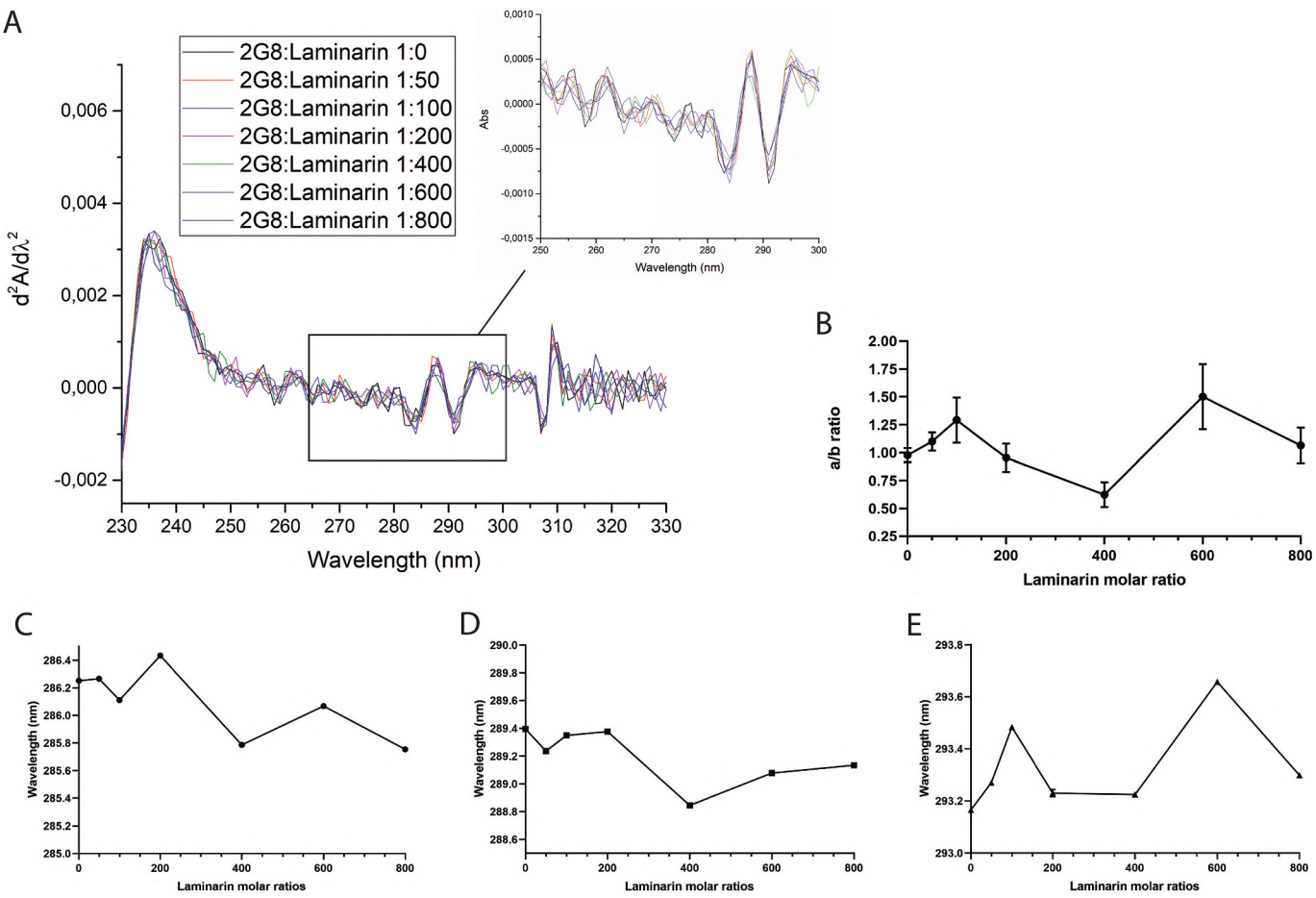

Fig. 4. Biophysical characterization of 2G8 using derivative spectroscopy. (A) Transformation of zero-order absorption spectra into second derivatives to resolve overlapping bands. (B) a/b ratio calculation from second-derivative spectra of 2G8 titrated with increasing molar ratio of laminarin. (C, D and E) Monitoring of wavelength shifts at the zero-crossing points. Shown spectral profiles are representative of three independent replicates. To ensure robust statistics, the a/b ratio and the abscissa intersection wavelengths were calculated for each individual measurement (n = 3) prior to averaging. Values are expressed as mean ± SD.

[49,50]. The biphasic nature of the spectral progression was confirmed also by the a/b ratio. The native a/b ratio for both antibodies approximates 1, consistent with a folded globular structure. Initial laminarin addition (1:50–1:100) increased the a/b ratio in both antibodies, signaling an increased solvent exposure of Tyrosine residues, typical of an opening or relaxation of the binding pocket. This was followed by a marked decrease in the ratio at intermediate concentrations (1:200–1:400), suggesting a re-burying of Tyr residues [51,52]. We attribute this biphasic progression to a mechanism of positive cooperativity driven by antibody bivalency. The data supports a model where the first binding event (1:50–1:100) induces a conformational change that facilitates the second interaction (1:200–1:400), effectively saturating the binding sites. The repetitive sequence of the β-1,3-glucan antigen likely stabilizes this cooperative bridging between paratopes. Spectral deviations at the highest molar ratios suggest subsequent non-specific interactions or structural distortions beyond the saturation point. Fig. 5 illustrates a simplified, schematic model of the binding mechanism of both antibodies linking the biphasic derivative changes to bivalent binding.

3.2. Far-UV circular dichroism (CD) spectroscopy and secondary structure analysis

The local spectroscopic behavior aligns perfectly with the secondary structure analysis *via* Far-UV CD spectroscopy. Spectra deconvoluted using the BeStSel algorithm resolved subtle variations in β-sheet topology. Both antibodies displayed characteristic IgG profiles dominated by β-sheet structures (positive peak at 202 nm, negative minimum at 215–216 nm) and with high antiparallel β-sheet content (42.0% for 2G8 and 48.4% for Dia-T51) in the native state (Fig. 6A and B and Table 1).

While the total β-sheet content remained invariant upon laminarin binding (molar ratio 1:200, (42.7% for 2G8 and 47.8% for Dia-T51), Dia-T51 underwent a coherent backbone reorganization: the "relaxed" antiparallel β-sheet fraction increased significantly at the expense of the "right-hand" and "left-hand twisted" fractions (Fig. 6C and D and Table 1).

Kinetically, both antibodies showed rapid binding (< 5 min), though with distinct spectral footprints: 2G8 exhibited marked variations at both 215 and 202 nm, whereas Dia-T51 changes were localized primarily to the positive peak (Fig. 6E and F). Two distinct populations - particularly visible at 215 nm -were identified based on spectral overlapping: an initial cluster at 1:10–1:150 M ratios and a second cluster at 1:200–1:300 M ratios (Fig. 6G). These findings reinforce the "induced fit" mechanism for Dia-T51, where the antibody scaffold adapts with a biphasic transition to accommodate the bulky laminarin antigen through local backbone and side-chain adjustments [53]. This plasticity likely contributes to the superior thermal stability of the Dia-T51 complex. In contrast, 2G8 lacks this backbone plasticity, forcing its aromatic residues into a complex, multiphasic struggle to bind the antigen, resulting in thermodynamic strain [54].

3.3. Thermal denaturation studies (CD thermoscans)

Thermal denaturation profiles were obtained by monitoring the CD

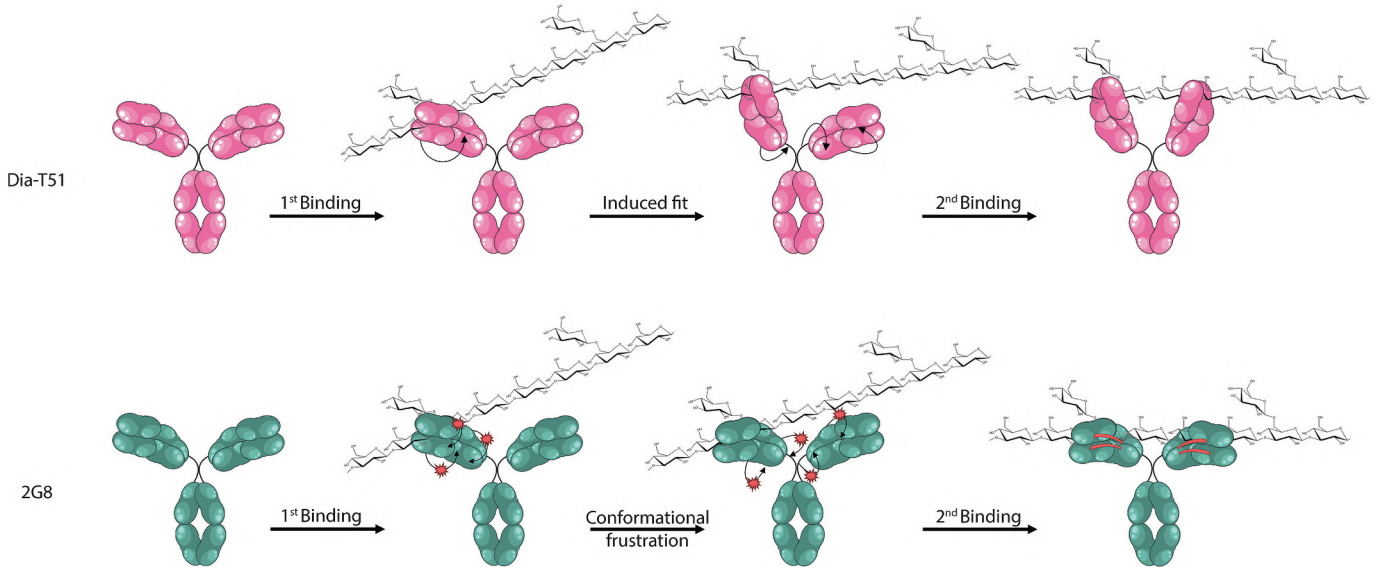

Fig. 5. Simplified schematic model of divergent binding strategies. Dia-T51 acts as a flexible scaffold. Upon initial engagement (1st Binding), it undergoes a coherent and coordinated structural reorganization (induced fit), to accommodate the bulky laminarin antigen. This plasticity enables the formation of a cooperative bivalent bridge (2nd Binding), highly stabilizing the complex and minimizing the overall thermodynamic cost. Conversely, 2G8 relies on a pre-organized, rigid paratope. The initial interaction fails to elicit cooperative adjustments. Because the inflexible scaffold cannot adapt, the molecule is driven into conformational frustration. This state, depicted by localized stress points and chaotic spatial rearrangements, hinders effective bivalent bridging, trapping the murine antibody in a strained conformation and imposing a significant energetic penalty.

signal from 20 °C to 100 °C (Fig. 7) and further quantified by calculating the apparent melting temperatures (Tm) (Table 2). Free Dia-T51 exhibited a broad thermal transition with an onset of aggregation/unfolding between 75 °C and 80 °C, culminating in a mathematically derived Tm of 83.28 °C. Conversely, the free 2G8 exhibited an earlier onset of thermal transition (65 °C–70 °C), although its global secondary structure loss yielded an apparent Tm of 91.51 °C. Complexation with laminarin exerted divergent thermodynamic effects, mirroring the structural mechanisms observed above. While Dia-T51 benefits from a massive stabilizing interaction with laminarin that dramatically delays the unfolding transition, shifting the Tm to an extraordinary 101.67 °C, the 2G8 complex manifests early structural destabilization and conformational instability (Tm of 90.10 °C). Moreover, for the 2G8 complex, significant spectral perturbations appear well below the melting temperature of the free antibody (~45 °C) [55]. Together, these quantitative data definitively confirm that the rigid, "frustrated" binding mode of 2G8 imposes a thermodynamic cost, whereas the localized plasticity and adaptive "induced fit" mode of Dia-T51 confers structural stability.

3.4. Binding affinity and kinetics

The binding affinity (K_D) was cross-validated using orthogonal methods, yielding constants in the nanomolar and sub-nanomolar range. Fluorescence spectroscopy for Dia-T51 yielded a steady-state K_D of 6.311 nM. Surface Plasmon Resonance (SPR) analysis determined a comparable K_D of 4.21 nM.

SPR kinetic analysis further resolved the interaction dynamics, providing a moderate association rate ($k_{on} = 1.44 \times 10^5\ M^{-1}\ s^{-1}$), and a highly stable dissociation phase ($k_{off} = 4.85 \times 10^{-4}\ s^{-1}$), resulting in a kinetic K_D of 3.37 nM (Fig. 8). While the approximately two-fold difference between the equilibrium and kinetic K_D values represents an excellent cross-platform agreement, this slight divergence is biophysically informative. It likely stems from a combination of phase differences - SPR operates at a 2D solid-liquid interface prone to transient micro-avidity effects, whereas fluorescence measures a 3D bulk solution - and the inherent heterogeneity of the polydisperse laminarin preparation. Furthermore, fitting the SPR data with a standard 1:1 L model represents an operational simplification: since Dia-T51 demonstrated to undergo a biphasic "induced fit" mechanism, the kinetic K_D is an apparent macroscopic affinity that complements the absolute thermodynamic equilibrium measured in solution. Overall, this robust kinetic profile, characterized by a moderate on-rate and highly stable off-rate, confirms the high specificity of the Dia-T51 interaction. In sharp contrast, 2G8 displayed a pronounced "fast-on" behavior. It yielded a steady-state K_D of 1.06 nM, but the most interesting information was obtained from the kinetic analysis. 2G8's exceptionally high association rate ($k_{on} = 1.28 \times 10^7\ M^{-1}\ s^{-1}$) drove an apparent overall higher affinity ($k_D = 0.25$ nM), fully compensating for a relatively faster off-rate ($k_{off} = 3.24 \times 10^{-3}\ s^{-1}$).

When integrated with the spectroscopic and thermal denaturation data, these kinetic parameters delineate two distinct thermodynamic strategies. The extraordinary k_{on} of 2G8 suggests a rigid, pre-organized paratope capable of instantaneous antigen engagement. However, as demonstrated by the multiphasic shifts in second-derivative UV spectroscopy and the early structural destabilization observed in CD thermoscans, this rapid docking forces the complex into a "conformational frustration". The rigid backbone of 2G8 lacks the necessary plasticity to properly accommodate the bulky laminarin, imposing a significant thermodynamic cost upon binding.

Conversely, the slower k_{on} of Dia-T51 reflects the energetic barrier associated with an "induced fit" mechanism. The antibody requires milliseconds to structurally adapt to the antigen: this data reinforces the thesis of a local plasticity confirmed also by the coordinated relaxation of its antiparallel β-sheets and the coherent biphasic structural response. However, once this initial energetic cost is paid, the resulting shape complementarity is near-perfect. Dia-T51 favors structural coherence and high and long-term stability over mere binding velocity. This translates into a very slow k_{off}, ultimately conferring the superior thermal resilience to the Dia-T51 complex.

3.5. In silico liability analysis and accelerated stability testing of Dia-T51

Moving toward translational potential and clinical feasibility, the resilience of Dia-T51 was evaluated under stress conditions. Prior to experimental stress testing, the Variable Light (VL) and Variable Heavy (VH) sequences of Dia-T51 were analyzed using ABodyBuilder2. This

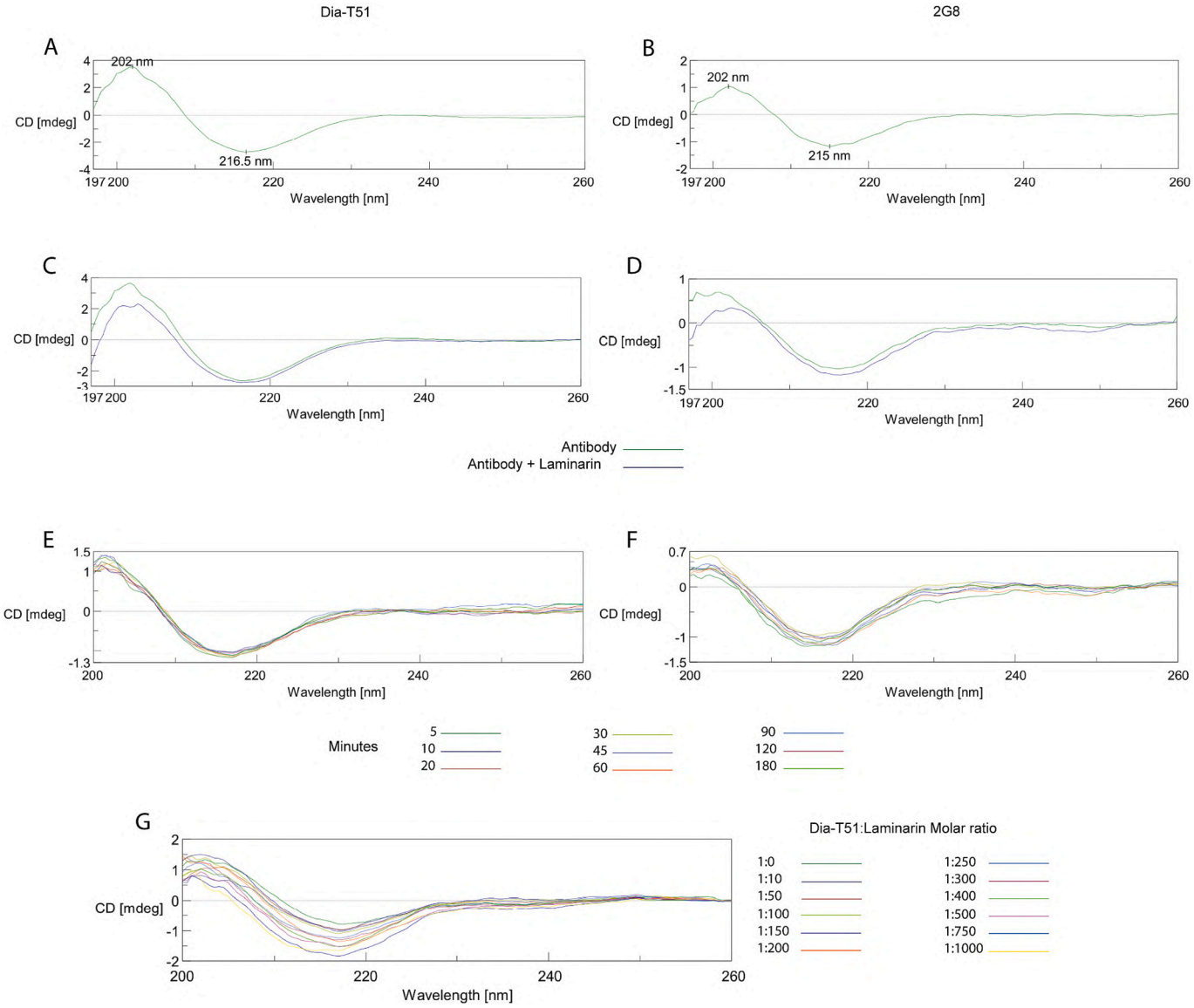

Fig. 6. Far-UV CD analysis of secondary structure of free and complexed antibodies. (A, B) Far-UV CD spectra of free Dia-T51 and 2G8, respectively. (C, D) Spectral analysis of secondary structure modifications of Dia-T51 and 2G8 respectively, upon laminarin binding. (E, F) Time-course analysis of Dia-T51 and 2G8 conformational changes due to antigen interaction. (G) Dose-dependent spectral evolution of Dia-T51 secondary structure upon addition of increasing amount of laminarin. Data are shown as a single representative profile selected from three independent replicates.

Table 1
Estimation of secondary structure content derived from Far-UV CD spectra deconvolution using the BeStSel algorithm. Data are reported as percentages.

Secondary structure	2G8	2G8 + Laminarin	Dia-T51	Dia-T51 + Laminarin
Regular α-helices	0	0	0	0
Distorted α-helices	2.1	1.5	0.5	1.5
Left-hand twisted antiparallel β-sheet	6.3	4.7	8.7	3
Relaxed/slightly right-hand twisted antiparallel β-sheet	19.7	20.7	16.3	25.3
Right-hand twisted antiparallel β-sheet	16.0	17.3	23.4	19.5
Parallel β-sheet	0	0	0	0
Turns	11.7	11.3	16.5	10.1
Others	44.3	42.8	34.7	40.7

machine learning-based antibody Fv modeling software was employed to predict structural liabilities at the amino acid level with high accuracy [30]. The model identified several residues potentially susceptible to chemical modifications, specifically oxidation, deamination, and isomerization, with a subset mapped directly to the Complementarity-Determining Regions (CDRs) (Table 3) [56–58].

The identification of these hotspots, especially those within the CDRs (CDR-H3-W109 and CDR-L1-NGNT34–37) initially raised concerns regarding potential functional impairment. In particular, Trp residues are sensitive to oxidative stress, which can lead to the formation of oxindolylalanine derivatives, potentially altering the hydrophobicity and conformational packing of the binding interface [56,59–61]. In parallel, the Asn-Gly (NG) motif is theoretically highly susceptible to the formation of a succinimide intermediate, leading to rapid deamidation [62–64]. However, as documented in several studies, a clear distinction must be made between "sequence-based liabilities" and "clinically relevant liabilities" [65]. In principle, even if these chemical modifications were to occur during stress, the functional integrity of Dia-T51 could be preserved through two potential stabilizing mechanisms.

The first concerns the functional redundancy of the paratope: high-

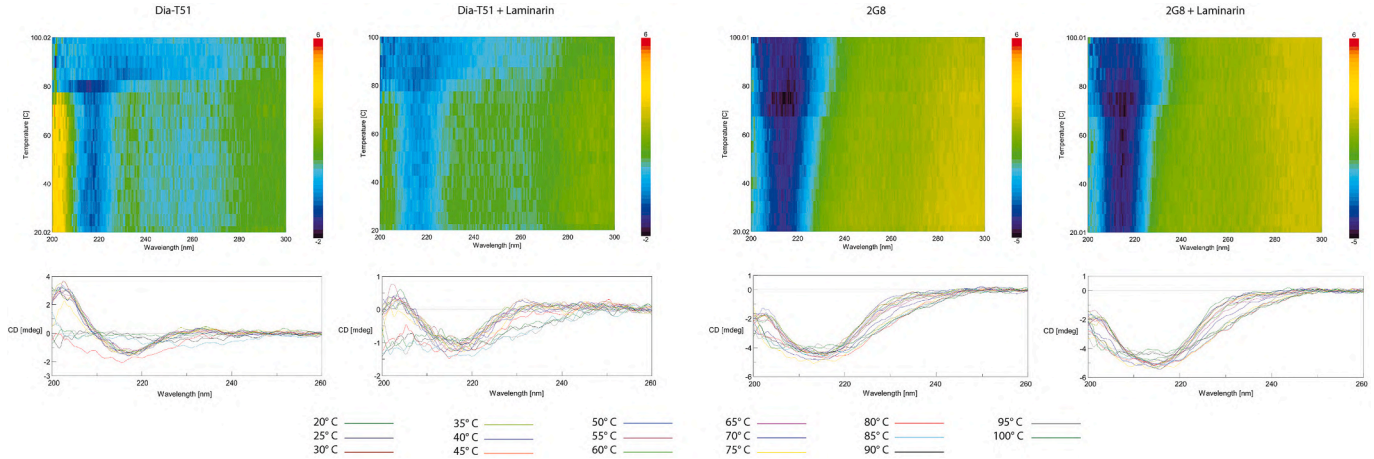

Fig. 7. Thermal denaturation profiles of free and complexed antibodies. Thermal stability was monitored by following the CD ellipticity at the negative peak from 20 °C to 100 °C. Traces represent one of three independent measurements yielding similar spectral profiles.

Table 2
Quantitative analysis of thermal stability *via* Far-UV CD-thermoscan. Apparent melting temperatures (Tm) were determined by monitoring the loss of secondary β-sheet structure at the negative peak (215–216.5 nm). The thermal shift (ΔTm) was calculated as the difference between the complexed and free states. Data represents the mean ± standard deviation of three independent measurements.

	Tm (°C)	± SD	ΔTm (°C)	± SD
Dia-T51	83.28	0.08	+18.39	1.65
Dia-T51 + Laminarin	101.67	1.65		
2 g8	91.51	1.15	−1.41	1.43
2 g8 + Laminarin	90.10	0.84		

affinity antibodies often possess a binding interface where only a fraction of the CDR residues, the "binding hotspots", contributes significantly to the free energy of interaction. Modifications to peripheral residues may be tolerated because they are not critical for antigen recognition [66,67]. The second mechanism regards structural shielding: residues can be protected if they are buried within the VH/VL interface or involved in a rigid hydrogen-bonding network that restricts the conformational flexibility required for oxidation or deamidation to proceed [62,68].To assess whether these predicted liabilities would compromise function over time [60,61,69], a sample from a 3-year-old stock of Dia-T51 (stored at 4 °C) was subjected to an accelerated stress test at 37 °C in PBS for up to 3 weeks - mimicking the physiological half-life -. Remarkably, functional analysis contradicted the pessimistic *in silico* predictions. During storage at 4 °C, Dia-T51 binding affinity was monitored after 6 and 12 months and led to a slight increase of IC_{50} compared to the freshly produced batch (0.10 μg/ml *vs* 0.06 μg/ml) while the kinetic K_D remained stable (3.37 10^{-9} M and 3.59 10^{-9} M). Even after the subsequent 3 weeks at 37 °C, Dia-T51 retained high antigen-binding capacity with an IC_{50} ~ 0.2 μg/ml, avg. K_D ~ 3.05 × 10^{-8} M and kinetic parameters close to the original baseline (Fig. 9A and B, and Table 4).

These results provide the experimental basis to categorize the previously identified hotspots as tolerated liabilities within the Dia-T51 architecture. Furthermore, no clinically relevant liabilities were observed under the tested conditions as no significant impairment of binding competence was detected. This implies that either the specific modifications were kinetically disfavored, or the Dia-T51 paratope possesses sufficient structural plasticity to tolerate such side-chain alterations without compromising antigen recognition.

While functional affinity was preserved, structural analysis provided insight into the physical cost of this stress. SDS-PAGE confirmed that the intact hmAb remained the predominant species, with only minor degraded fragments detected (Fig. 9C and D).

However, Dynamic Light Scattering (DLS) and spectroscopic data revealed signs of initial structural perturbation. DLS was employed to monitor the colloidal stability and aggregation/degradation state of Dia-T51 over time. The maintenance of the Polydispersity Index (PdI) values below 0.28 reflects a preserved homogeneity of the solution [70]. Deconvolution of the scattering signals identified three distinct peaks. Although minor populations of aggregates and fragments were detected (as evidenced by the secondary peaks), their low percentage contribution confirms that the antibody possesses a low propensity for self-association and precipitation, maintaining its monomeric state as the dominant species (Table 5).

Concurrently, UV and fluorescence spectra showed no significant wavelength shifts, suggesting the primary chromophore environment remained largely the same. However, a progressive and significant increase in fluorescence intensity was observed over the 37 °C incubation period (Fig. 10).

While degradation, misfolding and Tryptophan oxidation typically lead to quenching [71], the counter-intuitive increase in fluorescence intensity during stress testing suggests three potential mechanisms: (i) fragmentation releasing fluorophore-rich domains with higher quantum yields than in the native scaffold, (ii) the formation of soluble aggregates where altered inter- and intra-chromophore distances reduce native auto-quenching or (iii) a localized conformational rearrangement within the dominant scaffold that alters the microenvironment of the aromatic residues without involving a global exposure to the solvent [72].

These hypotheses align with DLS data, which detected a progressive increase in aggregate size, and are supported by Far-UV CD spectra, which revealed a deepening of the negative peak over time. The prolonged thermal stress drives a partial unfolding followed by reorganization into ordered cross β-structures (reminiscent of amyloid fibril precursors) as validated by BeStSel deconvolution (Table 6). The software detected an increase in β-sheet fraction and the appearance of non-native parallel β-sheets, a known structural hallmark of early-stage aggregation pathways [73]. However, since these initial observations were derived from a 3-year-old sample, it was crucial to distinguish whether this potential warning sign is an intrinsic liability of the Dia-T51 scaffold, or a consequence of extreme age-induced degradation coupled with thermal stress. To definitively resolve this, we performed a Congo Red spectroscopic binding assay and a proteolytic assay on a freshly produced antibody batch. Remarkably, and highly favorably for its translational potential, Dia-T51 showed no amyloidogenic propensity over a 14-day stress period (Fig. 11 and Table 7). The absorbance peak of Congo Red remained stable at ~490 nm with no trace of the characteristic aggregation-induced red shift. This is in stark contrast to our

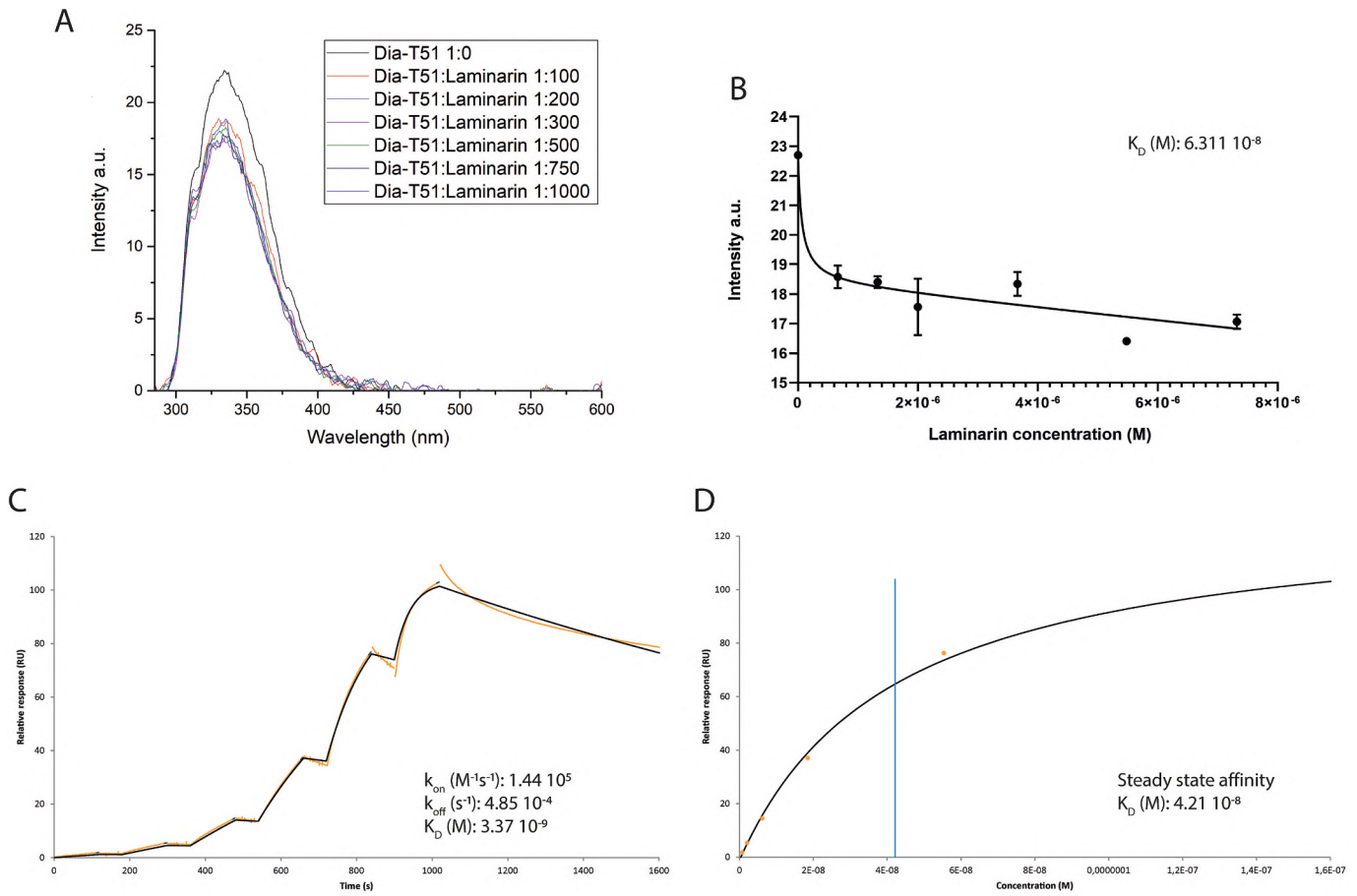

Fig. 8. Binding affinity determination of Dia-T51. (A-B) Fluorescence spectroscopy analysis showing raw spectral. The spectra are representative of n = 4 independent experiments and the values represent the mean ± SD of the four replicates. (C—D) SPR analysis illustrating the kinetic sensorgram and the steady-state affinity fit. Measurements were repeated 4 times.

Table 3
In silico prediction of structural liabilities within the Dia-T51 Variable Light (L) and Variable Heavy (H) chains using ABodyBuilder2. The table lists specific amino acid residues and their predicted susceptibility to chemical modifications. Residues located within the CDRs are marked with an asterisk (*).

Chain	Position	AA	Liability
H	38	W	Trp oxidation
	109*	W	
	118	W	
	4	M	Met oxidation
	41	W	Trp oxidation
	34*	N	Asn deamidation
	35*	G	
	36*	N	
	37*	T	
L	68	D	Asp isomerisation
	69	S	

positive control (heat-aggregated BSA), which displayed the expected prominent spectral shift to ~510 nm. Furthermore, the Abs540/Abs480 ratio remained strictly at baseline levels (~0.54) for Dia-T51, whereas it increased significantly for the aggregated BSA control (>1.1). According to established spectroscopic criteria [74], a ratio between 0.45 and 0.60 is characteristic of Congo Red in its monomeric, non-bound state, while values exceeding 1.0 indicate the characteristic red shift induced by binding to amyloid structures. Our results clearly show that Dia-T51 stays within the non-amyloidogenic range, whereas the heat-aggregated BSA control correctly reached the threshold indicative of aggregation.

As a consequence, the non-native parallel β-sheet signature detected in the aged stock does not represent an amyloid pathway but reflects a form of rearrangement driven by the extreme combination of long-term storage and subsequent thermal stress. Instead, the fresh batch confirms that the Dia-T51 sequence itself does not encode an intrinsic propensity for aggregate formation.

To further characterize the structural transitions observed in the fresh Dia-T51 batch - and confirm that it represents a stabilizing reorganization rather than a progression toward denaturation or aggregation -, we employed a proteolysis assay as an orthogonal probe (Fig. 12). Pepsin was used to map the solvent accessibility of the antibody backbone before and after a 10-day incubation at 37 °C. Consistent with the stability previously observed in our previous assays with the aged stock, undigested controls confirmed that the fresh Dia-T51 remains fully intact after thermal stress, providing a clean baseline prior to enzymatic treatment. The proteolytic fingerprints reveal a compelling kinetic shift especially under reducing conditions. In the unstressed sample (day 0), pepsin digestion is slower, with a prominent higher-molecular-weight band (>37 kDa) persisting even at the final time point (150 min). Following the 10-days incubation, pepsin completely digested that fragment making the band no longer detectable. Interestingly, on day 0, a low-molecular-weight fragment (<10 kDa) is already detectable after only 5 min of digestion; this same fragment is not yet visible in the 10-day stressed sample at the same time point. In summary, the stressed sample exhibits a delayed release of small fragments in the early stage of the assay but an increased proteolytic susceptibility in the later stages. These divergent kinetics demonstrate that structural reorganization does not lead to the formation of steric shields which typically hinder

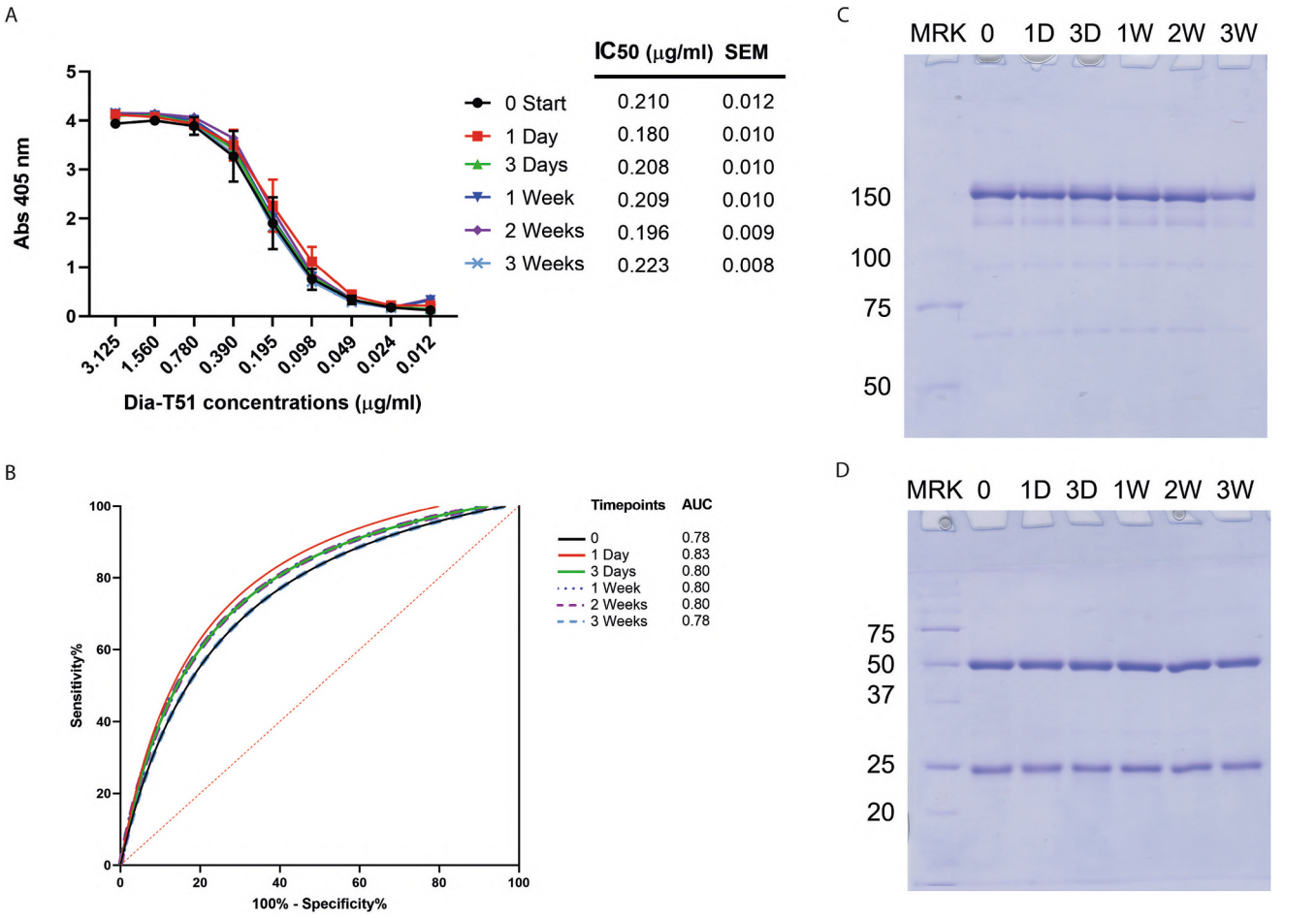

Fig. 9. Assessment of Dia-T51 functional stability and structural integrity. (A-B) Antigen-binding capability validated *via* ELISA and ROC curve analysis, demonstrating retained specificity. The data shown are the result of a technical triplicate. (C—D) SDS-PAGE analysis performed under non-reducing (C) and reducing (D) conditions and confirming the integrity of the antibody after 3 years and for the whole stability test.

Table 4
Evolution of kinetic parameters (k_{on}, k_{off}) and binding affinity (K_D) of Dia-T51 during the accelerated stability test. Values were determined *via* SPR at the indicated incubation time points at 37 °C.

Timepoints	kon	koff	KD
0	$1.26\ 10^{5}$	$1.09\ 10^{-2}$	$8.66\ 10^{-8}$
1 Day	$3.20\ 10^{5}$	$1.58\ 10^{-3}$	$4.95\ 10^{-9}$
3 Days	$5.3\ 10^{5}$	$4.33\ 10^{-3}$	$8.17\ 10^{-9}$
1 Week	$1.15\ 10^{5}$	$8.38\ 10^{-3}$	$7.26\ 10^{-8}$
2 Weeks	$2.58\ 10^{5}$	$1.39\ 10^{-3}$	$5.38\ 10^{-9}$
3 Weeks	$2.92\ 10^{5}$	$1.62\ 10^{-3}$	$5.55\ 10^{-9}$

enzymatic action. Instead, data suggests a subtle conformational refinement that initially protects certain cleavage sites while ultimately facilitates a more complete digestion of the antibody scaffold. Rather than collapsing into protease-resistant amyloid-like structures, in agreement with Congo Red assay results, the molecule undergoes a coherent transition toward a more dynamic yet controlled conformational state. The localized rearrangement alters the microenvironment of aromatic clusters, providing a mechanistic rationale for the counter-intuitive increase in fluorescence intensity previously observed. This increased flexibility prevents the accumulation of insoluble species and underscores the antibody's resilience under physiological stress.

Finally, these results indicate that while thermal stress induces substantial but localized secondary structure modifications, Dia-T51 maintains its overall globular architecture and remarkable functional

Table 5
Dynamic Light Scattering (DLS) analysis of Dia-T51 during the accelerated stability test. The table summarizes the *Z*-average diameter, Polydispersity Index (PdI), and the hydrodynamic diameter and area percentage for the three detected peaks. Values represent the mean of three independent measurements (consisting of 22 runs each) ± Standard Deviation (SD).

Timepoints	Z-Avg	SD	PdI	SD	Diameter (nm) Peak 1	SD	% Area Peak 1	SD	Diameter (nm) Peak 2	SD	% Area Peak 2	SD	Diameter (nm) Peak 3	SD	% Area Peak 3	SD
0	13.40	2.38	0,22	0.06	12.13	0.30	90.95	5.70	312.13	142.87	6.43	2.98	0.44	0.51	3.88	4.48
1 Day	23.90	13.29	0.22	0.09	12.91	0.32	88.44	3.28	292.44	43.31	10.34	1.78	0.16	0.36	1.14	2.55
3 Days	99.60	55.78	0.23	0.07	13.28	0.81	84.91	4.14	359.23	101.28	13.36	4.09	0.24	0.40	1.71	2.89
1 Week	14.05	3.28	0.28	0.08	12.36	0.29	90.26	3.93	338.11	55.75	7.94	1.90	0.23	0.40	1.80	3.08
2 Weeks	53.16	21.72	0.20	0.04	11.32	0.65	86.98	5.57	367.47	106.00	10.23	3.87	0.37	0.46	2.80	3.51
3 Weeks	40.84	28.26	0.15	0.05	10.97	0.46	89.52	7.94	338.33	214.63	5.36	2.73	0.32	0.41	4.95	8.88

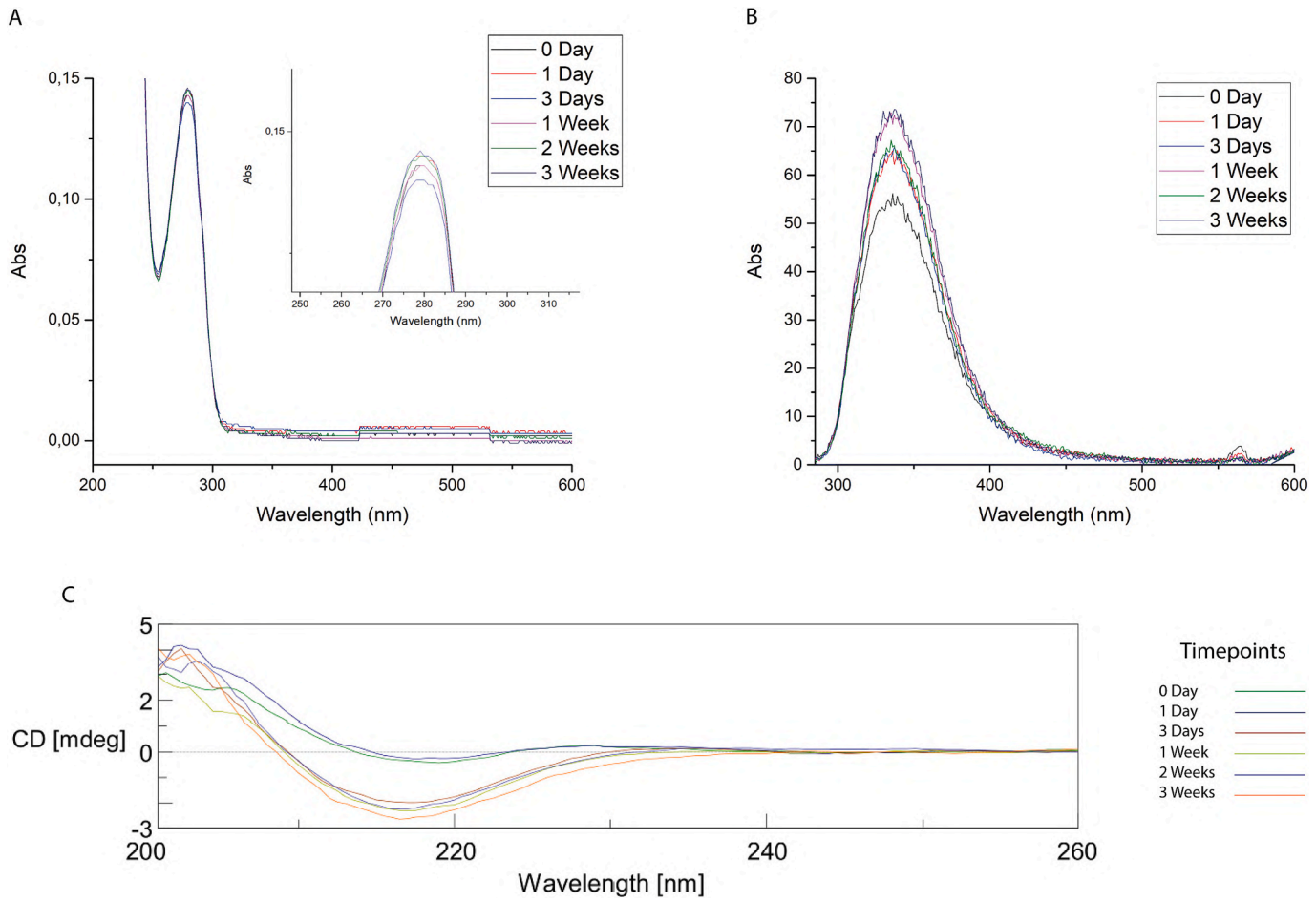

Fig. 10. Spectroscopic monitoring of Dia-T51 structural stability under accelerated stress. The panels illustrate the time-dependent evolution of (A) UV–Visible absorbance profiles, (B) intrinsic fluorescence emission spectra, and (C) Far-UV Circular Dichroism (CD) signatures collected throughout the thermal stress test. Measurements were performed three times.

Table 6
Time-dependent evolution of Dia-T51 secondary structure content during the accelerated stability test. Percentages of structural elements were estimated from Far-UV CD spectra using the BeStSel algorithm.

Secondary structure	Timepoints					
	0 day	1 day	3 days	1 week	2 weeks	3 weeks
Helix	0.7	1.8	0.0	0.0	0.0	0.0
Antiparallel β-sheet	50.8	46.4	66.9	62.5	57.5	59.8
Parallel β-sheet	0.0	3.1	8.4	12.7	5.3	5.8
Turs	16.5	5.8	16.2	6.0	9.0	8.0
Other	32.0	42.9	8.4	27.3	28.3	26.4

integrity. More importantly, the humanized mAb retains its binding capability even after 3 years of storage and despite these structural alterations, confirming its outstanding suitability for clinical development.

3.6. Study limitations

While the structural and functional resilience of Dia-T51 provides a compelling case for its drug-likeness, a balanced consideration of the study's limitations is essential to contextualize these findings within a broader clinical framework. A primary methodological constraint lies in the use of proteolytic probing with pepsin; although these assays successfully mapped backbone accessibility, the requirement for an acidic environment represents a significant difference from the physiological

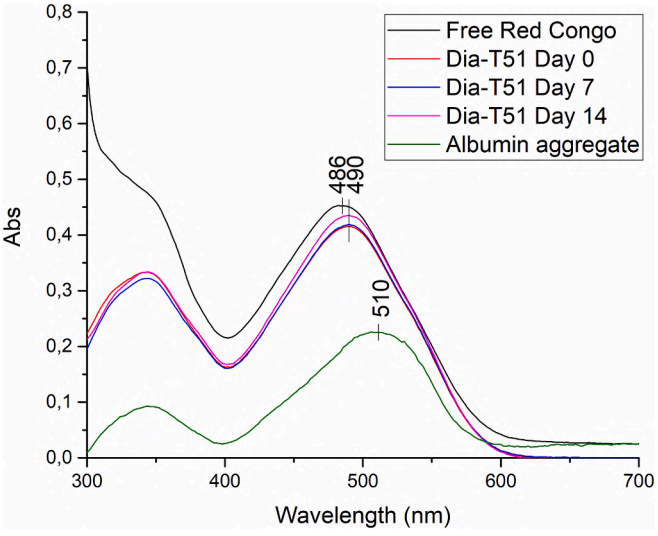

Fig. 11. Congo Red spectroscopic assay for amyloid detection. UV–Vis absorbance spectra of Congo Red free and bound to freshly produced Dia-T51 incubated at 37 °C for 0, 7, and 14 days. Heat-aggregated BSA was used as positive control. Shown data is the result of a technical triplicate.

conditions maintained during our thermal stress and binding evaluations. Consequently, the observed structural plasticity may be partially

Table 7
Congo Red spectral binding ratios. The Abs540/Abs480 ratio serves as a quantitative metric for amyloid formation. Baseline values between 0.45 and 0.60 indicate a non-aggregative state, whereas values >1.0 denote ordered cross-β fibrillization.

	Ratio Abs_{540}/Abs_{480}	± SD
Dia-T51 Day 0	0.541	0.0004
Dia-T51 Day 0	0.544	0.0037
Dia-T51 Day 0	0.542	0.0031
Albumine aggregate	1.145	0.1338

influenced by acid-induced conformational transitions that might not fully reflect the molecule's behavior at neutral pH. Furthermore, while the preservation of antigen-binding competence after prolonged stress identifies the CDR-hotspots as tolerated liabilities, this assessment remains inherently functional. The absence of site-specific quantification *via* high-resolution mass spectrometry means that the exact chemical transformation rates of specific residues remain unquantified, leaving open the possibility of silent degradation pathways that do not immediately impair affinity. Additionally, the use of laminarin, a naturally derived, polydisperse polysaccharide, introduces an inherent degree of heterogeneity that may influence the precision of kinetic determinations compared to a monodisperse, synthetic ligand.

In terms of developability, the current stability profile focuses on thermal challenge, whereas the industrial transition toward clinical batches will necessitate further evaluation of mechanical stresses, including interfacial agitation and freeze-thaw cycles which are critical parameters for formulation and long-term storage. Finally, while *in vitro* robustness is essential, it cannot fully predict the vv *in vivo* performance. Future investigations must evaluate Dia-T51 into complex biological matrices to determine the pharmacokinetics, clearance, and potential immunogenicity. Acknowledging these boundaries does not diminish the antibody's demonstrated stability but rather defines the necessary path to validate Dia-T51 as a safe and effective therapeutic agent.

4. Conclusion

In the quest to bridge the gap between “bench and bedside,” deep biophysical and biochemical profiling serves as the ultimate gatekeeper

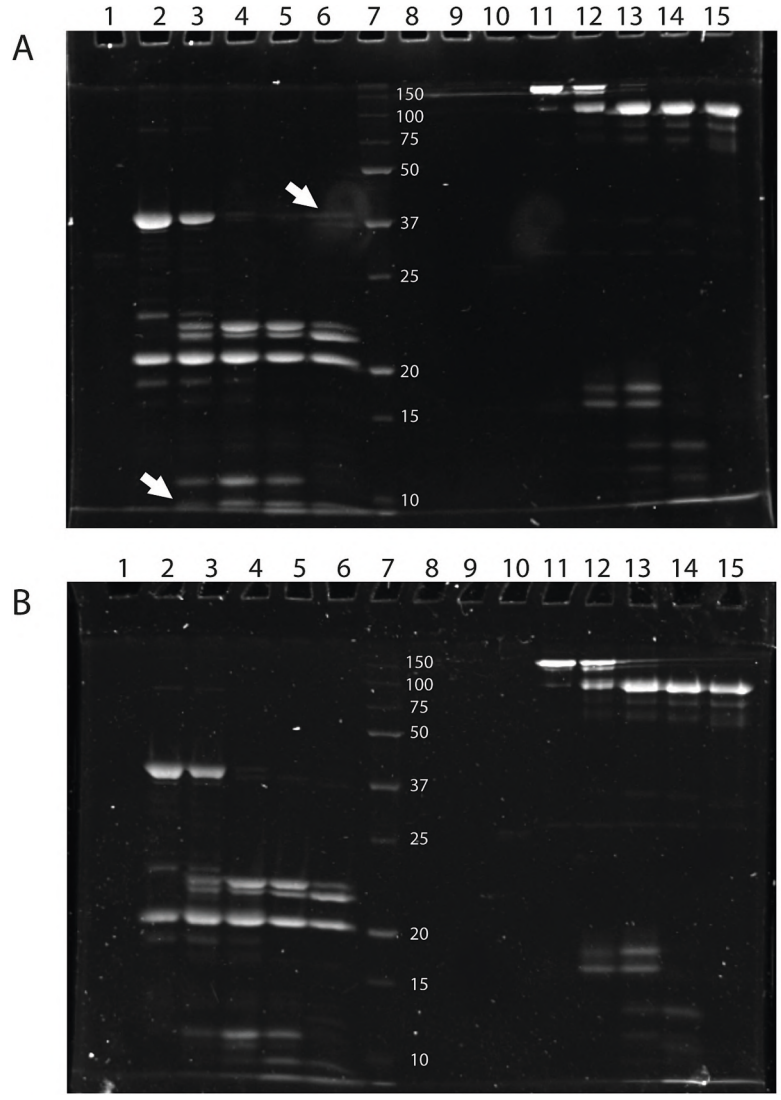

Well	Sample	Condition
1	Pepsin	Reduced with β-mercaptoethanol
2	Dia-T51 not digested	
3	Dia-T51 - 5 min. digestion	
4	Dia-T51 - 15 min. digestion	
5	Dia-T51 - 45 min. digestion	
6	Dia-T51 - 150 min. digestion	
7	Marker	
8	Sample buffer	
9	Sample buffer	
10	Pepsin	Not reduced
11	Dia-T51 not digested	
12	Dia-T51 - 5 min. digestion	
13	Dia-T51 - 15 min. digestion	
14	Dia-T51 - 45 min. digestion	
15	Dia-T51 – 150 min. digestion	

Fig. 12. Proteolysis mapping of Dia-T51. SDS-PAGE time-course of Dia-T51 digestion by pepsin under non-reducing and reducing conditions at day 0 (A) and after 10 days incubation at 37 °C (B). Undigested antibody and pepsin-only were used as controls. White arrows indicate the main differences in the banding pattern between the two gels: the upper arrow highlights the >37 kDa fragment, which is completely degraded at 150 min in the stressed sample; the lower arrow marks the delayed emergence of small fragments (<10 kDa) at 5 min. The backbone accessibility and the transition between dynamic conformational states rules out the formation of protease-resistant aggregates.

for antibody developability. This study establishes a comprehensive molecular blueprint for the humanized mAb Dia-T51, demonstrating that its structural architecture possesses the intrinsic robustness required for clinical translation. A fundamental strength of this work lies in the comparative understanding of the binding mechanisms: while the murine progenitor 2G8 suffers from "conformational frustration" and thermodynamic strain, Dia-T51 utilizes a cooperative "induced fit" strategy. This hallmark backbone plasticity, evidenced by coordinated β-sheet relaxation and biphasic UV-derivative shifts, allows Dia-T51 to pay the initial energetic cost of adaptation to achieve near-perfect shape complementarity. This translates into an extraordinary thermal stabilization of the complex, effectively transforming structural flexibility into a thermodynamic advantage. Furthermore, we have empirically de-risked the *in silico* liability profile through a unique combination of long-term aging and accelerated thermal stress. Our findings highlight that predicted chemical hotspots within the CDRs, often flagged as detrimental, can be effectively neutralized by the surrounding structural architecture. The preservation of nanomolar affinity and monomeric integrity under these extreme conditions confirms that such sequence-based liabilities remain functionally silent, likely due to structural shielding or paratope redundancy. This demonstrates that Dia-T51 avoids common degradation pathways, undergoing instead a stabilizing reorganization toward a more dynamic conformational state rather than collapsing into irreversible aggregates.

While these results are compelling, a balanced assessment requires acknowledging the study's inherent limitations. The reliance on functional assays to infer chemical stability, without site-specific mass spectrometry quantification, leaves minor degradation pathways unmapped. Methodologically, the acidic conditions required for proteolytic probing and the use of a naturally polydisperse antigen like laminarin introduce variables that may deviate from a purely physiological or monoclonal interaction baseline. Additionally, clinical developability will necessitate further resilience testing which were not addressed here.

Looking forward, the transition of Dia-T51 toward clinical use must now move into complex biological matrices to evaluate its pharmacokinetic profile, systemic clearance, and potential immunogenicity. Future research should prioritize high-resolution structural mapping of the antibody-antigen complex to further refine the "induced fit" model. Moreover, considering previous studies, exploring the interaction between Dia-T51 and antifungal agents represents an interesting avenue for future research. By validating its structural and functional "fitness", we have provided the evidence required to de-risk Dia-T51, offering a robust candidate for the next generation of resilient, high-affinity antifungal biotherapeutics.

CRediT authorship contribution statement

Tania Vanzolini: Writing – review & editing, Writing – original draft, Visualization, Validation, Supervision, Resources, Project administration, Methodology, Investigation, Funding acquisition, Formal analysis, Data curation, Conceptualization. **Valentina Fiori:** Writing – review & editing, Supervision, Resources, Project administration. **Tomas Di Mambro:** Writing – review & editing, Validation, Resources. **Mauro Magnani:** Writing – review & editing, Supervision, Resources, Project administration, Methodology, Funding acquisition, Conceptualization.

Declaration of Generative AI and AI-assisted technologies in the writing process

During the preparation of this work the authors used Google Gemini 1.5 (Generative AI tool, accessed January 2026) in order to improve the readability and flow of the manuscript's language. The tool was also employed to verify the syntax of specific command-line instructions used for the structural analysis software in ChimeraX. After using this tool/service, the authors reviewed and edited the content as needed and take full responsibility for the content of the published article.

Funding

This work was funded by the European Union – NextGenerationEU, Mission 4, Component 2, under the Italian Ministry of University and Research (MUR) National Innovation Ecosystem grant ECS00000041 - VITALITY – CUP H33C22000430006.

Declaration of competing interest

The authors declare the following financial interests/personal relationships which may be considered as potential competing interests: Tania Vanzolini reports equipment, drugs, or supplies was provided by Diatheva SRL. Mauro Magnani reports a relationship with Diatheva SRL that includes: equity or stocks. Valentina Fiori reports a relationship with Diatheva SRL that includes: employment. Tomas Di Mambro reports a relationship with Diatheva SRL that includes: employment. Tania Vanzolini has patent #WO2022096455A1 licensed to Diatheva SRL. Mauro Magnani has patent #WO2022096455A1 licensed to Diatheva SRL. Tomas Di Mambro has patent #WO2022096455A1 licensed to Diatheva SRL. Diatheva s.r.l. supported the study providing the humanized antibody Dia-T51 but was not involved in carrying out or managing the investigation, nor was it involved in the analysis and interpretation of data and in the preparation of the manuscript. M.M. holds shares in Diatheva s.r.l. V.F. and T.D.M. are employees of Diatheva s.r.l., T.V., T.D.M. and M.M. are inventors of Dia-T51 antibody as declared in patent WO2022096455A1 belonging to Diatheva s.r.l. This does not alter our adherence to the journal policies on sharing data and materials. If there are other authors, they declare that they have no known competing financial interests or personal relationships that could have appeared to influence the work reported in this paper.

Acknowledgements

The authors thank Diatheva s.r.l. for the production of the humanized monoclonal antibody Dia-T51 and the murine monoclonal antibody 2G8. We gratefully thank Prof. Luca Casettari and his research group for providing access to the DLS. The authors acknowledge the use of some Servier Medical Art image templates (https://smart.servier.com) in the preparation of Fig. 5. These elements are licensed under a Creative Commons Attribution 4.0 Unported License.

Data availability

All data generated or analyzed during this study are included in this manuscript text, tables, and figures.

References

[1] D.M. Ecker, S.D. Jones, H.L. Levine, The therapeutic monoclonal antibody market, mAbs 7 (2015) 9–14, https://doi.org/10.4161/19420862.2015.989042.
[2] J.M. Reichert, Antibodies to watch in 2010, mAbs 2 (2010) 84–100, https://doi.org/10.4161/mabs.2.1.10677.
[3] S. Crescioli, H. Kaplon, L. Wang, J. Visweswaraiah, V. Kapoor, J.M. Reichert, Antibodies to watch in 2025, mAbs 17 (2025) 2443538, https://doi.org/10.1080/19420862.2024.2443538.
[4] T. Jain, T. Sun, S. Durand, A. Hall, N.R. Houston, J.H. Nett, B. Sharkey, B. Bobrowicz, I. Caffry, Y. Yu, Y. Cao, H. Lynaugh, M. Brown, H. Baruah, L.T. Gray, E.M. Krauland, Y. Xu, M. Vásquez, K.D. Wittrup, Biophysical properties of the clinical-stage antibody landscape, Proc. Natl. Acad. Sci. 114 (2017) 944–949, https://doi.org/10.1073/pnas.1616408114.
[5] A. Jarasch, H. Koll, J.T. Regula, M. Bader, A. Papadimitriou, H. Kettenberger, Developability assessment during the selection of novel therapeutic antibodies, J. Pharm. Sci. 104 (2015) 1885–1898, https://doi.org/10.1002/jps.24430.
[6] H. Ma, C. Ó'Fágáin, R. O'Kennedy, Antibody stability: a key to performance - analysis, influences and improvement, Biochimie 177 (2020) 213–225, https://doi.org/10.1016/j.biochi.2020.08.019.

[7] P. Garidel, M. Hegyi, S. Bassarab, M. Weichel, A rapid, sensitive and economical assessment of monoclonal antibody conformational stability by intrinsic tryptophan fluorescence spectroscopy, Biotechnol. J. 3 (2008) 1201–1211, https://doi.org/10.1002/biot.200800091.

[8] S. Alavattam, B. Demeule, J. Liu, S. Yadav, M. Cromwell, S.J. Shire, Biophysical analysis in support of development of protein pharmaceuticals, in: L.O. Narhi (Ed.), Biophys. Ther. Protein Dev., Springer, New York, NY, 2013, pp. 173–204, https://doi.org/10.1007/978-1-4614-4316-2_8.

[9] D.W. Denning, Global incidence and mortality of severe fungal disease, Lancet Infect. Dis. 24 (2024) e428–e438, https://doi.org/10.1016/S1473-3099(23)00692-8.

[10] M.C. Fisher, A. Alastruey-Izquierdo, J. Berman, T. Bicanic, E.M. Bignell, P. Bowyer, M. Bromley, R. Brüggemann, G. Garber, O.A. Cornely, S.J. Gurr, T.S. Harrison, E. Kuijper, J. Rhodes, D.C. Sheppard, A. Warris, P.L. White, J. Xu, B. Zwaan, P. E. Verweij, Tackling the emerging threat of antifungal resistance to human health, Nat. Rev. Microbiol. 20 (2022) 557–571, https://doi.org/10.1038/s41579-022-00720-1.

[11] S.R. Lockhart, J. Guarner, Emerging and reemerging fungal infections, Semin. Diagn. Pathol. 36 (2019) 177–181, https://doi.org/10.1053/j.semdp.2019.04.010.

[12] T. Vanzolini, M. Magnani, Old and new strategies in therapy and diagnosis against fungal infections, Appl. Microbiol. Biotechnol. 108 (2024) 147, https://doi.org/10.1007/s00253-023-12884-8.

[13] P.G. Pappas, M.S. Lionakis, M.C. Arendrup, L. Ostrosky-Zeichner, B.J. Kullberg, Invasive candidiasis, Nat. Rev. Dis. Primer 4 (2018) 18026, https://doi.org/10.1038/nrdp.2018.26.

[14] N.A.R. Gow, J.-P. Latge, C.A. Munro, The fungal Cell Wall: structure, biosynthesis, and function, Microbiol. Spectr. 5 (2017), https://doi.org/10.1128/microbiolspec.FUNK-0035-2016.

[15] N. Kondori, L. Edebo, I. Mattsby-Baltzer, A novel monoclonal antibody recognizing β(1–3) glucans in intact cells of *Candida* and *Cryptococcus*, APMIS 116 (2008) 867–876, https://doi.org/10.1111/j.1600-0463.2008.01013.x.

[16] A.L. Matveev, V.B. Krylov, Y.A. Khlusevich, I.K. Baykov, D.V. Yashunsky, L. A. Emelyanova, Y.E. Tsvetkov, A.A. Karelin, A.V. Bardashova, S.S.W. Wong, V. Aimanianda, J.-P. Latgé, N.V. Tikunova, N.E. Nifantiev, Novel mouse monoclonal antibodies specifically recognizing β-(1→3)-D-glucan antigen, PLoS One 14 (2019) e0215535, https://doi.org/10.1371/journal.pone.0215535.

[17] A. Torosantucci, P. Chiani, C. Bromuro, F. De Bernardis, A.S. Palma, Y. Liu, G. Mignogna, B. Maras, M. Colone, A. Stringaro, S. Zamboni, T. Feizi, A. Cassone, Protection by anti-beta-glucan antibodies is associated with restricted beta-1,3 glucan binding specificity and inhibition of fungal growth and adherence, PLoS One 4 (2009) e5392, https://doi.org/10.1371/journal.pone.0005392.

[18] B.A. Keyt, R. Baliga, A.M. Sinclair, S.F. Carroll, M.S. Peterson, Structure, function, and therapeutic use of IgM antibodies, Antibodies 9 (2020) 53, https://doi.org/10.3390/antib9040053.

[19] A. Torosantucci, C. Bromuro, P. Chiani, F. De Bernardis, F. Berti, C. Galli, F. Norelli, C. Bellucci, L. Polonelli, P. Costantino, R. Rappuoli, A. Cassone, A novel glyco-conjugate vaccine against fungal pathogens, J. Exp. Med. 202 (2005) 597–606, https://doi.org/10.1084/jem.20050749.

[20] A. Rachini, D. Pietrella, P. Lupo, A. Torosantucci, P. Chiani, C. Bromuro, C. Proietti, F. Bistoni, A. Cassone, A. Vecchiarelli, An anti-beta-glucan monoclonal antibody inhibits growth and capsule formation of *Cryptococcus neoformans in vitro* and exerts therapeutic, anticryptococcal activity *in vivo*, Infect. Immun. 75 (2007) 5085–5094, https://doi.org/10.1128/IAI.00278-07.

[21] K.-I. Ishibashi, M. Yoshida, I. Nakabayashi, H. Shinohara, N.N. Miura, Y. Adachi, N. Ohno, Role of anti-beta-glucan antibody in host defense against fungi, FEMS Immunol. Med. Microbiol. 44 (2005) 99–109, https://doi.org/10.1016/j.femsim.2004.12.012.

[22] T. Di Mambro, T. Vanzolini, M. Bianchi, R. Crinelli, B. Canonico, F. Tasini, M. Menotta, M. Magnani, Development and *in vitro* characterization of a humanized scFv against fungal infections, PLoS One 17 (2022) e0276786, https://doi.org/10.1371/journal.pone.0276786.

[23] T. Di Mambro, T. Vanzolini, M. Magnani, Humanised antibodies against pathogenic fungi. https://patentscope2.wipo.int/search/en/detail.jsf;jsessionid=B46BC3B0DD407C2609CFC9470294510B?docId=WO2022096455&_gid=202219, 2022. (Accessed 12 December 2022).

[24] T. Di Mambro, T. Vanzolini, P. Bruscolini, S. Perez-Gaviro, E. Marra, G. Roscilli, M. Bianchi, A. Fraternale, G.F. Schiavano, B. Canonico, M. Magnani, A new humanized antibody is effective against pathogenic fungi *in vitro*, Sci. Rep. 11 (2021) 19500, https://doi.org/10.1038/s41598-021-98659-5.

[25] T. Vanzolini, V. Fiori, M. Magnani, *Candidozyma auris*-infected *galleria mellonella* larvae: the effect of the humanized monoclonal antibody Dia-T51 and its synergy with amphotericin B, Npj Antimicrob. Resist. 4 (2026) 25, https://doi.org/10.1038/s44259-026-00198-4.

[26] W. Zhang, H. Wang, N. Feng, Y. Li, J. Gu, Z. Wang, Developability assessment at early-stage discovery to enable development of antibody-derived therapeutics, Antib. Ther. 6 (2023) 13–29, https://doi.org/10.1093/abt/tbac029.

[27] A.-M. Wolf Pérez, N. Lorenzen, M. Vendruscolo, P. Sormanni, Assessment of therapeutic antibody Developability by combinations of *in vitro* and *in silico* methods, Methods Mol. Biol. 2313 (2022) 57–113, https://doi.org/10.1007/978-1-0716-1450-1_4.

[28] M.I.J. Raybould, C. Marks, K. Krawczyk, B. Taddese, J. Nowak, A.P. Lewis, A. Bujotzek, J. Shi, C.M. Deane, Five computational developability guidelines for therapeutic antibody profiling, Proc. Natl. Acad. Sci. U.S.A. 116 (2019) 4025–4030, https://doi.org/10.1073/pnas.1810576116.

[29] E.M. Moussa, J.P. Panchal, B.S. Moorthy, J.S. Blum, M.K. Joubert, L.O. Narhi, E. M. Topp, Immunogenicity of therapeutic protein aggregates, J. Pharm. Sci. 105 (2016) 417–430, https://doi.org/10.1016/j.xphs.2015.11.002.

[30] L.F. Willis, N. Kapur, S.E. Radford, D.J. Brockwell, Biophysical analysis of therapeutic antibodies in the early development pipeline, Biol. Targets Ther. 18 (2024) 413–432, https://doi.org/10.2147/BTT.S486345.

[31] P. Garidel, A.B. Kuhn, L.V. Schäfer, A.R. Karow-Zwick, M. Blech, High-concentration protein formulations: how high is high? Eur. J. Pharm. Biopharm. Off. J. Arbeitsgemeinschaft Pharm. Verfahrenstechnik EV 119 (2017) 353–360, https://doi.org/10.1016/j.ejpb.2017.06.029.

[32] Y. Le Basle, P. Chennell, N. Tokhadze, A. Astier, V. Sautou, Physicochemical stability of monoclonal antibodies: a review, J. Pharm. Sci. 109 (2020) 169–190, https://doi.org/10.1016/j.xphs.2019.08.009.

[33] A. Micsonai, F. Wien, É. Bulyáki, J. Kun, É. Moussong, Y.-H. Lee, Y. Goto, M. Réfrégiers, J. Kardos, BeStSel: a web server for accurate protein secondary structure prediction and fold recognition from the circular dichroism spectra, Nucleic Acids Res. 46 (2018) W315–W322, https://doi.org/10.1093/nar/gky497.

[34] A. Micsonai, F. Wien, L. Kernya, Y.-H. Lee, Y. Goto, M. Réfrégiers, J. Kardos, Accurate secondary structure prediction and fold recognition for circular dichroism spectroscopy, Proc. Natl. Acad. Sci. 112 (2015) E3095–E3103, https://doi.org/10.1073/pnas.1500851112.

[35] M.G. Bruque, A. Rodger, S.V. Hoffmann, N.C. Jones, J. Aucamp, T.R. Dafforn, O.R. T. Thomas, Analysis of the structure of 14 therapeutic antibodies using circular dichroism spectroscopy, Anal. Chem. 96 (2024) 15151–15159, https://doi.org/10.1021/acs.analchem.4c01882.

[36] P. Füglistaller, Comparison of immunoglobulin binding capacities and ligand leakage using eight different protein a affinity chromatography matrices, J. Immunol. Methods 124 (1989) 171–177, https://doi.org/10.1016/0022-1759(89)90350-5.

[37] P.L. Ey, S.J. Prowse, C.R. Jenkin, Isolation of pure IgG1, IgG2a and IgG2b immunoglobulins from mouse serum using protein a-sepharose, Immunochemistry 15 (1978) 429–436, https://doi.org/10.1016/0161-5890(78)90070-6.

[38] G. Rajauria, R. Ravindran, M. Garcia-Vaquero, D.K. Rai, T. Sweeney, J. O'Doherty, Molecular characteristics and antioxidant activity of laminarin extracted from the seaweed species *Laminaria hyperborea,* using hydrothermal-assisted extraction and a multi-step purification procedure, Food Hydrocoll. 112 (2021) 106332, https://doi.org/10.1016/j.foodhyd.2020.106332.

[39] B. Abanades, W.K. Wong, F. Boyles, G. Georges, A. Bujotzek, C.M. Deane, ImmuneBuilder: deep-learning models for predicting the structures of immune proteins, Commun. Biol. 6 (2023) 575, https://doi.org/10.1038/s42003-023-04927-7.

[40] J. Dunbar, K. Krawczyk, J. Leem, T. Baker, A. Fuchs, G. Georges, J. Shi, C. M. Deane, SAbDab: the structural antibody database, Nucleic Acids Res. 42 (2014) D1140–D1146, https://doi.org/10.1093/nar/gkt1043.

[41] B. Lee, F.M. Richards, The interpretation of protein structures: estimation of static accessibility, J. Mol. Biol. 55 (1971) 379–IN4, https://doi.org/10.1016/0022-2836(71)90324-X.

[42] C. Chothia, The nature of the accessible and buried surfaces in proteins, J. Mol. Biol. 105 (1976) 1–12, https://doi.org/10.1016/0022-2836(76)90191-1.

[43] H. Mach, C.R. Middaugh, Simultaneous monitoring of the environment of tryptophan, tyrosine, and phenylalanine residues in proteins by near-ultraviolet second-derivative spectroscopy, Anal. Biochem. 222 (1994) 323–331, https://doi.org/10.1006/abio.1994.1499.

[44] A.B. Biter, J. Pollet, W.-H. Chen, U. Strych, P.J. Hotez, M.E. Bottazzi, A method to probe protein structure from UV absorbance spectra, Anal. Biochem. 587 (2019) 113450, https://doi.org/10.1016/j.ab.2019.113450.

[45] D.S. Katayama, R. Nayar, D.K. Chou, J. Campos, J. Cooper, D.G. Vander Velde, L. Villarete, C.P. Liu, M. Cornell Manning, Solution behavior of a novel type 1 interferon, interferon-tau, J. Pharm. Sci. 94 (2005) 2703–2715, https://doi.org/10.1002/jps.20461.

[46] L.J. Waters, J. Whiteley, W. Small, S. Mellor, Determining suitable surfactant concentration ranges to avoid protein unfolding in pharmaceutical formulations using UV analysis, Heliyon 9 (2023) e21712, https://doi.org/10.1016/j.heliyon.2023.e21712.

[47] T. Ichikawa, H. Terada, Second derivative spectrophotometry as an effective tool for examining phenylalanine residues in proteins, Biochim. Biophys. Acta 494 (1977) 267–270, https://doi.org/10.1016/0005-2795(77)90154-4.

[48] D.U. Ferreiro, J.A. Hegler, E.A. Komives, P.G. Wolynes, Localizing frustration in native proteins and protein assemblies, Proc. Natl. Acad. Sci. 104 (2007) 19819–19824, https://doi.org/10.1073/pnas.0709915104.

[49] Y. Nozaki, Determination of tryptophan, tyrosine, and phenylalanine by second derivative spectrophotometry, Arch. Biochem. Biophys. 277 (1990) 324–333, https://doi.org/10.1016/0003-9861(90)90587-o.

[50] C. Balestrieri, G. Colonna, A. Giovane, G. Irace, L. Servillo, Second-derivative spectroscopy of proteins. A method for the quantitative determination of aromatic amino acids in proteins, Eur. J. Biochem. 90 (1978) 433–440, https://doi.org/10.1111/j.1432-1033.1978.tb12622.x.

[51] S. Birtalan, Y. Zhang, F.A. Fellouse, L. Shao, G. Schaefer, S.S. Sidhu, The intrinsic contributions of tyrosine, serine, glycine and arginine to the affinity and specificity of antibodies, J. Mol. Biol. 377 (2008) 1518–1528, https://doi.org/10.1016/j.jmb.2008.01.093.

[52] R. Ragone, G. Colonna, C. Balestrieri, L. Servillo, G. Irace, Determination of tyrosine exposure in proteins by second-derivative spectroscopy, Biochemistry 23 (1984) 1871–1875, https://doi.org/10.1021/bi00303a044.

[53] J.M. Rini, U. Schulze-Gahmen, I.A. Wilson, Structural evidence for induced fit as a mechanism for antibody-antigen recognition, Science 255 (1992) 959–965, https://doi.org/10.1126/science.1546293.
[54] L.C. James, D.S. Tawfik, Conformational diversity and protein evolution – a 60-year-old hypothesis revisited, Trends Biochem. Sci. 28 (2003) 361–368, https://doi.org/10.1016/S0968-0004(03)00135-X.
[55] V. Joshi, T. Shivach, N. Yadav, A.S. Rathore, Circular dichroism spectroscopy as a tool for monitoring aggregation in monoclonal antibody therapeutics, Anal. Chem. 86 (2014) 11606–11613, https://doi.org/10.1021/ac503140j.
[56] S. Gupta, W. Jiskoot, C. Schoneich, A. Rathore, Oxidation and deamidation of monoclonal antibody products: potential impact on stability, biological activity, and efficacy, J. Pharm. Sci. 111 (2021), https://doi.org/10.1016/j.xphs.2021.11.024.
[57] X. Lu, R.P. Nobrega, H. Lynaugh, T. Jain, K. Barlow, T. Boland, A. Sivasubramanian, M. Vásquez, Y. Xu, Deamidation and isomerization liability analysis of 131 clinical-stage antibodies, mAbs 11 (2018) 45–57, https://doi.org/10.1080/19420862.2018.1548233.
[58] J.A. Pavon, L. Xiao, X. Li, J. Zhao, D. Aldredge, E. Dank, A. Fridman, Y.-H. Liu, Selective tryptophan oxidation of monoclonal antibodies: oxidative stress and modeling prediction, Anal. Chem. 91 (2019) 2192–2200, https://doi.org/10.1021/acs.analchem.8b04768.
[59] J.A. Pavon, L. Xiao, X. Li, J. Zhao, D. Aldredge, E. Dank, A. Fridman, Y.-H. Liu, Selective tryptophan oxidation of monoclonal antibodies: oxidative stress and modeling prediction, Anal. Chem. 91 (2019) 2192–2200, https://doi.org/10.1021/acs.analchem.8b04768.
[60] T. Hageman, H. Wei, P. Kuehne, J. Fu, R. Ludwig, L. Tao, A. Leone, M. Zocher, T. K. Das, Impact of tryptophan oxidation in complementarity-determining regions of two monoclonal antibodies on structure-function characterized by hydrogen-deuterium exchange mass spectrometry and surface Plasmon resonance, Pharm. Res. 36 (2019) 24, https://doi.org/10.1007/s11095-018-2545-8.
[61] T. Dashivets, J. Stracke, S. Dengl, A. Knaupp, J. Pollmann, J. Buchner, T. Schlothauer, Oxidation in the complementarity-determining regions differentially influences the properties of therapeutic antibodies, mAbs 8 (2016) 1525–1535, https://doi.org/10.1080/19420862.2016.1231277.
[62] J.F. Sydow, F. Lipsmeier, V. Larraillet, M. Hilger, B. Mautz, M. Mølhøj, J. Kuentzer, S. Klostermann, J. Schoch, H.R. Voelger, J.T. Regula, P. Cramer, A. Papadimitriou, H. Kettenberger, Structure-based prediction of asparagine and aspartate degradation sites in antibody variable regions, PLoS One 9 (2014) e100736, https://doi.org/10.1371/journal.pone.0100736.
[63] N.E. Robinson, A.B. Robinson, Prediction of protein deamidation rates from primary and three-dimensional structure, Proc. Natl. Acad. Sci. U.S.A. 98 (2001) 4367–4372, https://doi.org/10.1073/pnas.071066498.
[64] Y. Yan, S. Tang, S. Wang, N. Li, Assessing the impact of CDR Deamidation and isomerization on mAb target binding using affinity-resolved 2D-SEC-SCX-MS analysis, J. Am. Soc. Mass Spectrom. 36 (n.d.) 2682–2691. doi:https://doi.org/10.1021/jasms.5c00284.
[65] T. Satława, M. Tarkowski, S. Wróbel, P. Dudzic, T. Gawłowski, T. Klaus, M. Orłowski, A. Kostyn, S. Kumar, A. Buchanan, K. Krawczyk, LAP: liability antibody profiler by sequence & structural mapping of natural and therapeutic antibodies, PLoS Comput. Biol. 20 (2024) e1011881, https://doi.org/10.1371/journal.pcbi.1011881.
[66] A.A. Bogan, K.S. Thorn, Anatomy of hot spots in protein interfaces, J. Mol. Biol. 280 (1998) 1–9, https://doi.org/10.1006/jmbi.1998.1843.
[67] I. Sela-Culang, V. Kunik, Y. Ofran, The structural basis of antibody-antigen recognition, Front. Immunol. 4 (2013), https://doi.org/10.3389/fimmu.2013.00302.
[68] X. Lu, R.P. Nobrega, H. Lynaugh, T. Jain, K. Barlow, T. Boland, A. Sivasubramanian, M. Vásquez, Y. Xu, Deamidation and isomerization liability analysis of 131 clinical-stage antibodies, mAbs 11 (2019) 45–57, https://doi.org/10.1080/19420862.2018.1548233.
[69] R. Garg, S. McCarthy, A.G. Thompson, J. Zhang, E. Mattson, A. Clabbers, A. Acquah, J. Xu, C. Zhou, A. Ali, D. Filoti, R. Singh, *In vitro* stability study of a panel of commercial antibodies at physiological pH and temperature as a guide to screen biologic candidate molecules for the potential risk of *in vivo* asparagine Deamidation and activity loss, Pharm. Res. 42 (2025) 353–363, https://doi.org/10.1007/s11095-025-03825-3.
[70] J. Stetefeld, S.A. McKenna, T.R. Patel, Dynamic light scattering: a practical guide and applications in biomedical sciences, Biophys. Rev. 8 (2016) 409–427, https://doi.org/10.1007/s12551-016-0218-6.
[71] K. Zheng, D. Ren, Y.J. Wang, W. Lilyestrom, T. Scherer, J.K.Y. Hong, J.A. Ji, Monoclonal antibody aggregation associated with free radical induced oxidation, Int. J. Mol. Sci. 22 (2021) 3952, https://doi.org/10.3390/ijms22083952.
[72] M.V. Khan, S.M. Zakariya, R.H. Khan, Protein folding, misfolding and aggregation: a tale of constructive to destructive assembly, Int. J. Biol. Macromol. 112 (2018) 217–229, https://doi.org/10.1016/j.ijbiomac.2018.01.099.
[73] S. Basha, D.C. Mukunda, A.R. Pai, K.K. Mahato, Assessing amyloid fibrils and amorphous aggregates: a review, Int. J. Biol. Macromol. 311 (2025) 143725, https://doi.org/10.1016/j.ijbiomac.2025.143725.
[74] E.I. Yakupova, L.G. Bobyleva, I.M. Vikhlyantsev, A.G. Bobylev, Congo red and amyloids: history and relationship, Biosci. Rep. 39 (2019) BSR20181415, https://doi.org/10.1042/BSR20181415.